

NATIONAL BUREAU OF STANDARDS  
MICROCOPY RESOLUTION TEST CHART

AD-A158 088

FUNDAMENTAL STUDIES ON THE  
ALUMINUM-LITHIUM-BERYLLIUM ALLOY  
SYSTEM

J. Wadsworth

LMSC-F035827

July 1985

DTIC FILE COPY

SELECTED  
AUG 14 1985  
S A

 **Lockheed Missiles & Space Company, Inc.**  
SUNNYVALE, CALIFORNIA

This document has been approved  
for public release and sale; its  
distribution is unlimited.

85 7 22 058 *hth*

## TABLE OF CONTENTS

<u>Section</u>		<u>Page</u>
1	<u>Introduction</u>	1
2	<u>Experimental Procedures</u>	4
3	<u>Results and Discussion</u>	5
3.1	Arc Cast Alloys	6
3.2	Compositional Variations in Al-3Li-10Be Arc Melted Button	7
3.3	Splat Quenched Al-Li-Be Alloys	9
3.4	Melt Spun Al-Li-Be Alloys	11
	A) <u>Consolidated Ribbon</u>	13
	i) Al-3Li-2Be	14
	ii) Al-3Li-10Be	15
	B) <u>Tensile Tested Condition</u>	15
	C) <u>Surface Oxides on Melt Spun Ribbon</u>	16

ACKNOWLEDGMENTS

REFERENCES

Accession For	
NTIS GRA&I	<input checked="" type="checkbox"/>
DTIC TAB	<input checked="" type="checkbox"/>
Unannounced	<input type="checkbox"/>
<i>Letter on file</i>	
By _____	
Distribution _____	
Availability Codes	
Dist _____	Special
A-1	



2

FUNDAMENTAL STUDIES ON THE  
ALUMINUM-LITHIUM-BERYLLIUM ALLOY  
SYSTEM

J. Wadsworth

LMSC-F035827

July 1985

*N00014-84-C-0032*

First Year Report

to

Office of Naval Research

Arlington, Virginia

Lockheed Palo Alto Research Laboratory  
Lockheed Missiles & Space Company, Inc.  
3251 Hanover Street  
Palo Alto, CA 94304

AUG 14 1985

This document has been approved  
for public release and sale; its  
distribution is unlimited.

## 1. Introduction

A considerable effort has been expended in recent years in the development of advanced aluminum alloys. Two major areas of work have evolved<sup>(1,2)</sup>. The first area is directed toward the production of high modulus alloys, predominantly for use at high temperature, using rapid solidification processing (RSP) and powder metallurgy (PM) consolidation. These alloys are based on the Al-Mn and Al-Fe systems. The second area, in recognition of the overriding importance of low density in weight savings in aerospace structures<sup>(3)</sup>, is the development of low density and high modulus alloys based on the aluminum-lithium system<sup>(4,5)</sup>. These Al-Li alloys are predominantly manufactured using ingot metallurgy techniques although successful PM alloys have also been produced<sup>(6)</sup>.

In order to take further advantage of density decreases in aluminum alloys, it is not possible simply to continue to increase the lithium content of the alloy. Beyond a level of about 3 wt.%, deleterious effects of lithium are observed on toughness and ductility. In the search for other elements that can decrease density it is important to note that associated decreases in modulus are not desirable. As a result of this restriction, it can be determined that only two elemental additions to aluminum have the effect of simultaneously decreasing density and increasing the elastic modulus by significant amounts<sup>(7,8)</sup>. These are lithium and beryllium; Li is both the most efficient density-decreasing and modulus-increasing of all metallic elements when added to aluminum. The combination of Li and Be in Al has not been attempted before because of the low solid solubility of Be in Al (<0.03 percent by weight, as shown in Figure 1)<sup>(8)</sup>. This low solubility results in massive segregation of the Be-rich phase upon solidification under standard conditions, and this leads to poor mechanical properties.

↓ RSP + Li

Rapid solidification processing (RSP) is a unique and potentially practical method for the development of high modulus and high strength microstructures in Al-Li alloys containing more than about 0.03 percent Be. The RSP would eliminate segregation of Be and greatly refine the microstructure of the alloy. The addition of Li further reduces the density significantly and at the same time increases the elastic modulus and strength. The successful development of Al-Li-Be alloys would result in ultra-low density, high modulus and high strength Al alloys, competing with the most promising metal-matrix and non-metal matrix composites with respect to weight savings in advanced aerospace structures. The potential for weight savings in such structures is significantly higher for Al-Li-Be alloys than for any other Al alloy system, including composites. In previous work<sup>(3)</sup>, it was shown that weight savings in aerospace structures depend on a variety of properties, the principal one being density, followed by elastic modulus and then strength. The addition of Be and Li both lower the density and increase the modulus of Al, as described above. In a preliminary study of Al-Li-Be alloys<sup>(9)</sup> using the S-3A Naval Patrol Aircraft as a structural example<sup>(3,6)</sup>, the weight savings were calculated for two illustrative Al-Li-Be compositions: Al-3Li-3Be and Al-3Li-10Be<sup>(9)</sup>. The results, together with similar calculations (made using experimental data<sup>(10-12)</sup>) for other advanced aluminum alloys, as well as for a metal-matrix composite<sup>(13)</sup>, have clearly demonstrated the important benefits obtainable by the Al-Li-Be alloys. For example, by comparison with Al-7075, an Al-3Li-10Be alloy exhibited a 26% weight savings and an Al-3Li-3Be a 20% weight savings. A 7000 series 20 vol.% SiC alloy would have a 22% weight savings whereas the novel Al-Li based alloys range from 8 to 14% weight savings. The Al-Li-Be alloys are therefore a group of alloys which could have applications in aerospace structural components resulting in major increases in range, payload and service life.

Because of the limited solubility of Be in Al, alloys based on the Al-Be system constitute an important case for the application of the RSP technique. At low temperature, although Be has only a small solid solubility in Al, at increased temperatures, Figure 1, it shows an increasing liquid solubility, reaching approximately 10 percent by weight at  $1000^{\circ}\text{C}$ <sup>(8)</sup>. Therefore, it should be possible to obtain by rapid solidification a microstructure in which the aluminum solid solution contains a high concentration of fine discrete particles of Be or of a Be-rich phase. These particles can have three important effects upon the mechanical properties of the aluminum alloys: 1) a decrease in density, 2) an increase of the elastic modulus, and 3) an increase in strength. In order to achieve a significant room temperature strength contribution from the Be phase dispersoids, it would be necessary to avoid excessive coarsening of this phase during metallurgical processing. However, it has been shown<sup>(14)</sup> that Al-Be binary alloys produced by RSP and having up to 10 percent Be have a fine dispersion of alpha Be particles. Upon subsequent heat treatment the particles showed some coarsening but remain with average sizes smaller than 100 nm.

In Al alloys containing both Li and Be, produced by RSP, two phases are expected to form precipitates. The  $\text{Al}_3\text{Li}$  ( $\delta'$ ) phase is expected to precipitate as fine, coherent spheroids which will provide a significant contribution to strength<sup>(10)</sup>. The Be-rich phase is expected to precipitate in the form of a dispersoid within the Al-Li matrix. This Be-rich phase will contribute to the mechanical properties of the alloy in two different way: 1) by adding a dispersion strengthening component to the yield strength, and 2) by acting to disperse dislocation glide, which will allow the  $\text{Al}_3\text{Li}$  phase to contribute more of its full potential to the alloy strength. It has been shown that very fine dispersoids provide a beneficial effect on improving the dispersion

of slip in Al-Li alloys. Because the  $Al_3Li$  ( $\delta'$ ) coherent precipitates are small (2 to 100 nm, depending upon aging condition) and their misfit with the aluminum lattice is small (less than 0.1 percent), they are readily sheared by dislocations and slip can occur by planar glide in Al-Li alloys containing more than about 1 wt.% Li. Both the limited ductility and low fracture toughness of various Al-Li alloys have been broadly attributed to this planar glide mechanism<sup>(11)</sup>. There are no known intermetallic compounds between Li and Be<sup>(15)</sup> and so it is expected that these elements will co-exist in an alloy without the formation of undesirable phases.

The purpose of this paper is to describe recent work on Al-Li-Be ternary alloys containing about 3 wt.% Li and up to 10 wt.% Be. The structure and properties of alloys after rapid solidification processing will be described.

## 2. Experimental Procedures

The materials used for manufacturing the Al-Li-Be ternary alloys were: pure Al (99.95%) from high purity ingot stock; high-purity battery-grade Li containing less than 1000 ppm of Na (and typically less than 300 ppm of Na), and electrolytic induction melted Be stock (99.6%) the main impurities being  $O_2$ , Fe, and Al. The Al was cleaned by chemically etching in a mixture of  $HNO_3$  and HF. The Li was handled in a low humidity (<1%) room, and the Be was cleaned by chemical etching in dilute  $H_2SO_4$ .

In order to make Al-Li-Be ternaries, master alloys of Al-Be were initially prepared by arc melting. The arc melting was carried out in a small depression in a water cooled Cu hearth in a chamber containing an Ar atmosphere. A getter button of pure Ti was melted prior to melting the small (20g) charges

of Al and Be, in order to remove as much as possible of N and O. The small castings of Al-Be thus produced were remelted several times (inverting the solidified ingot on each occasion) to promote homogeneity. These master alloys were chemically cleaned prior to the addition of Li which was made by placing the elemental Li underneath the Al-Be arc melted buttons, and slowly melting the Li by conduction from the top side of the buttons (at which point the arc was located). This procedure avoided evaporative losses of Li as the element diffuses into the master alloy prior to the mass becoming molten. This molten pool was puddled for several minutes, allowed to solidify and then the button was remelted three times.

A number of analyses on these arc melted buttons were carried out, primarily by optical metallography and Auger electron spectroscopy. Because of the severe segregation that was observed using optical metallography, it was necessary to determine the precise compositions at locations within the button from which samples for splat quenching could be machined. This was carried out using Auger electron spectroscopy.

Rapid solidification experiments were carried out using splat quenching and melt spinning. For the splat quenching experiments, small cubes (50-100 mg) were removed from the castings and splat quenched after melting with an arc in a hammer-anvil apparatus. In this device, a spring loaded Cu hammer, triggered with a solenoid release, is used to create a splat from the small molten pool. Melt spun ribbon was manufactured using an apparatus described elsewhere<sup>(9)</sup>.

### 3. Results and Discussion

#### 3.1 Arc Cast Alloys

Typical castings produced by arc-melting, of a range of Al-Li-Be alloys, are shown in Figure 2. Generally, a rather thick oxide surface was observed on each alloy. Upon sectioning, it was revealed that macrosegregation was apparent in each of the castings, but much more severely so in the case of the highly alloyed compositions. Examples of the coarse macrostructures of two of the alloys are given in Figure 3. As may be seen, the Al-3Li-10Be alloy showed an especially segregated structure; it was subsequently determined that the upper part of the casting (the light area of Figure 3(b)) was rich in Li. A small degree of porosity was also evident in some of the castings. Three castings (Al-3Li-2Be, Al-3Li-5Be, and Al-3Li-10Be) were investigated using optical microscopy and one was investigated (Al-3Li-10Be) for compositional details using Auger electron spectroscopy.

Because of the degree of segregation, it is difficult to present representative microstructures of each alloy. The structure varied considerably depending upon the precise location within the casting. Examples from each of the three compositions are illustrated in Figure 4(a), (b), and (c) at increasing magnifications. In Figure 5 optical photomicrographs are shown from within one of the castings (the Al-3Li-10Be composition). Despite the variation in structure within individual castings, some general observations can be made from Figures 4 and 5. As for the case of Al-Be binary alloys, the Be in the Al-Li-Be alloys is extremely insoluble and precipitates upon cooling from the melt in coarse, segregated form in a variety of irregular shapes and sizes. This is the predominant phase visible in Figures 4 and 5. This primary Be has

a large size range from about 2 to 70  $\mu\text{m}$ . Within these segregated regions, a cellular structure exists and at the cell walls are found both the Be-phase as well as, presumably, the Li containing phases (assumed to be  $\delta'$  or  $\delta$ ). This type of microstructure is most undesirable from the viewpoint of mechanical properties and provides the driving force to produce these compositions of Al-Li-Be alloys by RSP. Furthermore, because of the uncertainty of the compositional ranges within these castings, it was not possible to simply cut pieces for splat quenching experiments and assume nominal compositions. A detailed Auger analysis was therefore carried out to measure the composition fluctuations in a polished half-section of the Al-3Li-10Be alloy ingot in order to locate precisely regions for further study.

### 3.2 Compositional Variations in Al-3Li-10Be Arc Melted Button

A common procedure in preparation of alloy splats involves making a master alloy button (or casting) of a nominal composition and then using a small portion (e.g., a cube of side 0.1") of it to remelt and rapidly solidify by splatting. A source of composition fluctuation in splats arises from any inhomogeneity present in the master alloy button. The composition of the alloy can also change during each melting step due to evaporation losses and oxidation. These losses can be particularly high for Li and Be, leaving the splat deficient in these elements. Thus, an assurance of homogeneity in the master alloy, and careful melting practice to avoid oxidation and evaporation losses are important factors in achieving alloy splats of the desired composition. This section of the study was aimed at understanding the nature of macrosegregation present in the master alloy and is considered an essential step in preparing splats with preselected compositions.

The alloy with a nominal composition of Al-3Li-10Be was selected for this macrosegregation study. This is the alloy with the greatest Be and Li concentrations and was expected to be the most inhomogeneous among the various alloys studied. The macrosegregation study was conducted on a polished thin slice, shown in Figure 6, which was cut from the master alloy button.

The technique of Auger Electron Spectroscopy (AES) was used in evaluation of the lateral compositional inhomogeneity of the alloy. A Perkin-Elmer model PHI 560 ESCA/SAM system was used which has a minimum electron beam diameter of 1  $\mu\text{m}$ . In practice, the Scanning Auger Microprobe (SAM) electron beam was rastered to cover large areas of 400  $\mu\text{m}$  x 400  $\mu\text{m}$ . AES spectra and selected energy region multiplexes were obtained from various regions of the alloy slice and quantitative estimates made using elemental sensitivity factors. These quantitative estimates may have a  $\pm 30\%$  relative error for most elements and possibly larger errors for lithium concentrations. The errors in Li estimates are larger due to its peak occurring in the very low energy range (36-43 eV), which is also dominated by true secondary electrons. The large errors also arise due to changes in chemical states, e.g., when the elements are present in their oxide forms or mixed states. Attempts at better quantification are currently being made utilizing x-ray photoelectron spectroscopy (XPS) for large area (>5mm diameter) surface analysis and Inductively Coupled Plasma (ICP) for high accuracy bulk analysis. Surface analysis efforts using AES does offer a combination of attributes for the present study that include: (i) light element sensitivity with the exception of H and He, (ii) high lateral resolution as low as 2000 $\text{\AA}$ , (iii) surface sensitivity (5-20 $\text{\AA}$  region of the surface), (iv) depth profiling capability in conjunction with ion sputtering and, (v) chemical state information such as needed in distinguishing oxide states from elemental states.

AES estimates of Al, Be, Li, and oxygen concentrations were obtained from the areas shown in Figure 6. These data were obtained after sputter cleaning of surfaces to remove atmospheric oxides and contamination. The top portion of the button, represented by the light area of Figure 6, had a mottled appearance. An AES spectrum (Figure 7) obtained from area *d* within this region indicated high concentrations of Li, determined to be present in the form of an oxide (based upon its peak position). The estimated atomic concentrations from various locations marked in Figure 6 are shown in Table 1. The data

TABLE 1

AES COMPOSITIONAL ESTIMATES FROM VARIOUS LOCATIONS SHOWN IN FIGURE 6

<u>AREA/LOCATION*</u>	<u>ATOMIC %</u>				<u>COMMENTS</u>
	<u>Al</u>	<u>Be</u>	<u>Li</u>	<u>O</u>	
1	53	34	13	-	
2	45	41	13	1	
3	43	46	10	1	
4	38	36	17	10	
5	41	53	5	1	
6	23	70	3	4	
7	21	68	9	2	
8	25	68	4	2	
9	38	44	16	2	
1(a)*	76	10	13	1	Dark Phase
1(b)*	35	53	11	-	Light Phase
1(c)*	26	63	11	-	Light Phase
Bulk Concentration	68	23	9	-	

\*1(a) through 1(c) represent 20  $\mu\text{m}$  x 20  $\mu\text{m}$  areas. All others are 400  $\mu\text{m}$  x 400  $\mu\text{m}$  areas.

clearly indicates substantial variations in Li and Be concentrations at the various locations. It is generally found that Li is richer near the top surface of the button and in a form combined with oxygen. On the other hand, Be is enriched near the bottom of the button in concentrations estimated to be as high as 70 atomic percent. Even though the absolute quantities may be in large error, it is valid to conclude that large scale macrosegregation occurs during the preparation of these master alloy buttons. Hence, caution must be

- [8] Aluminum, Vol. 1, Properties, Physical Metallurgy and Phase Diagrams, ASM, K. R. Van Horn, Ed., 1968.
- [9] A. E. Vidoz, D. D. Crooks, R. E. Lewis, I. G. Palmer, and J. Wadsworth, ASTM STP on Rapidly Solidified Al Alloys, In Press, 1985.
- [10] I. G. Palmer, R. E. Lewis, and D. D. Crooks, "Development of Al-Li-X Alloys Using Rapidly Solidified Powders", Proc. 1982 AIME Conf. on Aluminum Powder Metall., Dallas, Texas, Feb. 1982, p. 369.
- [11] E. A. Starke, Jr., T. A. Sanders, Jr., and I. G. Palmer, "New Approaches to Alloy Development in the Al-Li System", J. Metals, 33, (8), 1981, p. 24.
- [12] H. G. Parris, F. R. Billman, W. S. Cebulak and J. I. Petit, Proc. Second Int. Conf. on Rapid Solidification Processing, Mar. 1980, R. Mehrabian, B. H. Kear, and M. Cohen, Eds., Claitors Publishing Div., Baton Rouge, LA, 1980, p. 331.
- [13] H. Rack, private communication, AORCO Metals Co., SILAG Operation, Greer, South Carolina, 1983.
- [14] L. Tanner, private communication, Lawrence Livermore Laboratory, Livermore, CA, 1983.
- [15] R. P. Elliot, Constitution of Binary Alloys, 1st Suppl., McGraw Hill, 1965, p. 65.
- [16] D. C. Van Aken and H. L. Fraser, Acta Metall., 33, 1985 p. 963.

## REFERENCES

- [1] J. R. Pickens, "Aluminum Powder Metallurgy Technology for High Strength Applications", J. Mater. Sci., 16, 1981, p. 1437.
  
- [2] T. E. Tietz and I. G. Palmer, "Advanced PM Aluminum Alloys", Proc. 1981 ASM Materials Science Seminar, Advances in Powder Technology, Louisville, Kentucky, Oct. 1981, p. 189.
  
- [3] J. C. Ekvall, J. E. Rhodes, and G. C. Wald, "Methodology for Evaluating Weight Savings from Basic Materials Properties", ASTM STP 761, Amer. Soc. for Testing and Materials, Philadelphia, PA, 1982, p. 328.
  
- [4] E. A. Starke, Jr., and T. H. Sanders, Jr., Eds., "Aluminum-Lithium Alloys", Proc. First Int. Al-Li Conf., AIME, Warrendale, PA (1981).
  
- [5] E. A. Starke, Jr., and T. H. Sanders, Jr., Eds., "Aluminum-Lithium Alloys II", Proc. Second Int. Al-Li Conf., AIME, Warrendale, PA (1983).
  
- [6] R. E. Lewis, I. G. Palmer, J. C. Ekvall, I. F. Sakata, and W. E. Quist, "Aerospace Structural Applications of Rapidly Solidified Aluminum-Lithium Alloys", Proc. Third Conference on Rapid Solidification Processing: Principles and Technology, Gaithersburg, MD, Dec. 6-8, 1982, p. 615.
  
- [7] I. G. Palmer, R. E. Lewis, and D. D. Crooks, "Low Density, High Modulus Aluminum-Lithium Alloys from Splat Particulate", Proc. Second Int. Conf. on Rapid Solidification Processing, Mar. 1980, R. Mehrabian, B. H. Kear, and M. Cohen, Eds., Claitors Publishing Div., Baton Rouge, LA, 1980, p. 342.

## ACKNOWLEDGMENTS

The author wishes to acknowledge Dr. D. Polk of the Office of Naval Research for funding this work under Navy Contract N00014-84-C-0032. The author is also most grateful to Dr. A. E. Vidoz and Mr. R. E. Lewis for their many contributions, to Dr. A. Joshi for Auger electron spectroscopy studies, to Dr. A. R. Pelton for transmission electron microscopy studies, and to Mr. D. D. Crooks for manufacture of the alloys.

savings over the complex Al-Li-Cu-Mg alloys. These comparisons assume the strength of the Al-Li-Be alloys is only 448 MPa, and with any increase in actual strength above that value, significant additional weight savings would be obtained.

significantly higher for aluminum-lithium alloys when additions of beryllium are considered. The weight savings depend on a variety of properties, the principal one being density, followed by the elastic modulus and strength<sup>(3)</sup>. The addition of beryllium both lowers the density and increases the modulus of aluminum-lithium alloys as shown in Table 2. Using the

TABLE 2  
DENSITY AND MODULUS VALUES OF SOME Al-Li AND Al-Li-Be ALLOYS

		Elastic (E) Modulus GPa (10 <sup>6</sup> psi)	Density (ρ) 10 <sup>3</sup> Kgm <sup>-3</sup> (1b in <sup>3</sup> )	Δ(E/ρ) (%)	Figure of Merit <sup>+</sup>
Al-2.8Li-0.14Zr	*	80.5 <sup>++</sup> (11.7)	2.49 <sup>++</sup> (0.090)	26.6	40.3
Al-3.0Li	*	83.2 <sup>++</sup> (12.1)	2.48 <sup>++</sup> (0.090)	31.3	44.9
Al-4.0Li	*	86.0 <sup>++</sup> (12.5)	2.40 <sup>++</sup> (0.087)	40.3	56.0
Al-4.4Li-1.2Zr	*	85.0 <sup>++</sup> (12.3)	2.42 <sup>++</sup> (0.087)	37.5	52.9
Al-2.8Li-0.14Zr-5.0Be		95.2 (14.4)	2.44 (0.088)	52.7	65.4
Al-3.0Li-5.0Be		97.7 (14.2)	2.44 (0.088)	56.8	68.9
Al-4.0Li-5.0Be		100.3 (14.5)	2.36 (0.085)	66.4	79.6
Al-4.4Li-1.2Zr-5.0Be		99.4 (14.4)	2.38 (0.086)	63.5	76.5
Al-2.8Li-0.14Zr-10.0Be		109.9 (15.9)	2.40 (0.086)	79.3	89.5
Al-3.0Li-10.0Be		112.3 (16.3)	2.39 (0.086)	84.0	93.5
Al-4.0Li-10.0Be		114.7 (16.6)	2.32 (0.084)	93.6	103.2
Al-4.4Li-1.2Zr-10.0Be		113.8 (16.5)	2.34 (0.084)	90.4	100.2

\* With respect to Al 7075  
 + Figure of Merit is  $\Delta E + 2.5 (-\Delta\rho)$   
 ++ Experimental result

S-3A Naval Patrol Aircraft as a structural example, the weight savings were calculated for two illustrative Al-Be-Li alloys: Al-3 wt.% Be - 3 wt.% Li and Al-3 wt.% Li - 10 wt.% Be, using techniques previously developed by Lockheed Corporation<sup>(9)</sup> and assuming densities of 2.43 and 2.38 g/cm<sup>3</sup>, respectively, and Young's Modulus of 93.1 and 112.4 GPa, respectively. The results showed that the Al-Li-Be alloys appear to provide about twice the weight

Aluminum is present in the entire oxide, but in much lower proportions than in the bulk. In some of the specimens, particularly those ribbons subsequently oxidized at 500°C for 20 minutes in air, a lithium-rich oxide was present at the surface followed by a well defined layer of beryllium-rich oxide. The total oxide thicknesses varied in the range of 100-500Å for the as-spun ribbons while the thicknesses varied in the 2.5 to 3 μm range for the oxidized specimens. Examples of the depth profiles of the as spun and oxidized specimens are shown in Figures 28 and 29, respectively. The layering of the Li- and Be-rich oxides upon oxidation at 500°C is demonstrated in Figure 29. The atomic concentration estimates (ordinate in these plots) should be used only on a relative basis since they were derived using elemental sensitivity factors and are subject to large errors.

The data clearly indicates preferential oxidation of Li and Be in the alloy. An examination of the free energies of formation of the metal oxides shown in Figure 30 suggests that BeO is the most stable oxide followed by Li<sub>2</sub>O and Al<sub>2</sub>O<sub>3</sub>. The experimental evidence of ready formation of LiO<sub>x</sub> at the surface, and its ease of formation relative to Al<sub>2</sub>O<sub>3</sub>, suggests that kinetic factors play an important role in formation of these surface oxides. Lithium rich surface oxides have readily formed due to rapid diffusion of Li through the oxide layer; this is as opposed to purely thermodynamic factors which would favor Beryllium oxides.

The role of these surface oxides on the agglomeration behavior of comminuted particulates and their effect on microstructure and mechanical properties of processed material will be included as part of future investigations.

The potential for weight savings in aerospace structures such as aircraft is

tamination, can have a profound influence on particulate agglomeration behavior and the contingent mechanical and chemical properties of the final compact. Hence, a thorough understanding of the ribbon surface species including oxides is desirable in understanding of material properties and microstructure. The nature and thickness of surface oxides of RSP ribbons or particulates is strongly influenced by the alloying elements, the rate of cooling from the melt and the partial pressures of  $H_2O$ ,  $O_2$  and other reactive gases during their preparation and storage. Also, handling and storage procedures including the vacuum/ambient quality can alter the amounts and nature of organic contamination.

The Al-3Li-2Be and Al-3Li-10Be melt spun ribbons were selected for investigations of the nature of surface oxides. The specimens were subjected to surface analysis in the as-spun condition and also after being subsequently oxidized at  $500^{\circ}C$  for 20 minutes in room air and reexamined (in order to determine the tendency for formation of equilibrium surface oxides). The technique of Auger Electron Spectroscopy (AES) was utilized for all the surface analyses as it offered (i) the desired surface sensitivity ( $<5-20\text{\AA}$ ), (ii) sensitivity for light elements including Li, Be, and O, (iii) chemical state information to determine whether the elements are present as oxides, (iv) high lateral resolution and (v) capability of depth profiling using inert gas ion sputtering. All the studies were conducted in a Perkin Elmer model PHI 560 ESCA/SAM system.

AES survey spectra obtained from the surfaces of various ribbons showed enrichment of C, O, Li, and Be at the surface. The composition-depth profiles obtained by argon ion sputtering indicated that carbon is generally localized in the top  $100-300\text{\AA}$  followed by a lithium and beryllium rich oxide layer.

As expected, the major difference between the samples in the T5 condition and those in the T6 strained condition is the increased dislocation density. The visibility of the dislocations, of course, depends on the diffraction conditions of the particular region. There was not any clear indication of particle ( $\alpha$ -Be or  $\delta'$ ) dislocation interactions in the samples examined in this study.

For the Al-3Li-2Be alloy, following the observation in the aged condition, the grains are not, in general, elongated. There are large grains with isolated regions containing smaller subgrains as shown in Figure 24. There are large depleted zones at the grain boundaries (i.e., devoid of  $\delta'$  particles). Again, the  $\alpha$ -Be has mainly precipitated at the grain boundaries of these smaller grains, and is dispersed throughout the larger grains. The PFZ's are particularly evident in the BF/WBDF pair of Figure 25 (using a  $\delta'$  reflection). At present, there is no clear reason why there are the depleted zones within the grains. Some of these regions could be  $\alpha$ -Be but not all of them can be.

For the case of the Al-3Li-10Be alloy in the T6 and tensile tested condition, there are many Be particles as shown in Figure 26. While the grains may not appear to be elongated, many of them are. The large  $\alpha$ -Be particle in Figure 27 is of particular interest. The small precipitates on the  $\alpha$ -Be particle could be small  $\alpha$ -Be particles. This type of precipitate has previously been observed by Fraser, et al<sup>(16)</sup> and by Tanner<sup>(14)</sup> in Al-Be binary alloys. The CBED pattern in Figure 27 is a typical one for this type of precipitation.

### C) Surface Oxides on Melt Spun Ribbons

The surface oxides and hydroxides on melt spun ribbon, as well as organic con-

evident in Figure 19. (As will be seen, such regions do not occur in the Al-3Li-10Be alloy, possibly due to the presence of a much greater volume fraction of  $\alpha$ -Be particles.) Furthermore, in both Figures 18 and 19 there appears to be intense deformation zones (the black areas in Figure 18 are regions of high defect density) associated with the  $\alpha$ -Be particles. A high magnification BF/WBDF pair (using a  $\delta'$  rejection) is shown in Figure 20. The  $\alpha$ -Be particles do not appear using this reflection but their location can be inferred by the low density of  $\delta'$  in these regions. The  $\delta'$  particles are about 20-50 nm in size (by comparison, particles of 5-10 nm are observed in the melt spun ribbon).

ii) Al-3Li-10Be

In this alloy, the grains were generally observed to be elongated with large angle grain boundaries along the longitudinal axis and generally small angle boundaries perpendicular to them. An example is shown in the TEM collage of Figure 21. The large volume fraction of  $\alpha$ -Be particles is also evident. These particles are both on grain boundaries and within grains and have, in some cases, very specific orientation relationships with the matrix. A region from within the overview microstructure of Figure 21 is shown in Figures 22 and 23, at low and high magnifications, respectively. In addition to the large  $\alpha$ -Be particles (left hand side of Figure 22), some agglomeration of the smaller Be particles has occurred during the processing for consolidation. This is clearly seen in Figure 23 in a region adjacent to a boundary.

B) Tensile Tested Condition

The above samples were also examined in the gage length after tensile testing.

niques were employed for this purpose. In Figure 17(c) a higher magnification image of a 200 nm particle is shown with a convergent beam microdiffraction pattern formed by focusing a 100 nm probe ( $\alpha_1 = 1.5$  mrad) on the precipitate. The [111] and [020]-type reflections from the [101] zone axis pattern of the Al matrix are outlined; the remaining low angle diffraction intensities are from the particle. In general, these precipitates are randomly oriented within the grains indicating that they formed prior to the solidification of the Al matrix. This is also commonly observed in splat quenched hypereutectic Al-Be alloys.

#### A) Consolidated Ribbon

Ribbons of both the Al-3Li-Be and Al-3Li-10Be alloys were converted into extruded bar using techniques previously described<sup>(9)</sup>. Tensile samples were fabricated from these bars, heat treated to an approximate T6 condition and tensile tested. In this section a transmission electron microscopy study of these alloys in the T6 condition and in the deformed T6 (tensile tested) condition is presented. Transmission electron microscopy samples were taken from samples such that the thin foil lay parallel to the original extrusion direction. In general, coarsening of the  $\alpha$ -Be particles from a size of less than 100 nm to the size range of 100 to 500 nm was observed to have taken place as a result of consolidation.

##### i) Al-3Li-2Be

Rather inhomogeneous structures were observed in these samples. For example, in Figures 18 and 19, TEM collages from adjacent regions within the same sample are shown. In Figure 18 there is no elongated grain structure as is

tion was carried out. Thinning of the ribbons for TEM was done in an electrolyte of 5% perchloric acid, 35% 2-butoxyethanol, and 60% methanol at 10°C with an applied potential of 15V and a resultant current of 75 mA. The samples were examined with JEOL 100CX TEM-STEM at 120 kV.

Figure 17(a) is a bright field/weak-beam dark field pair showing a typical microstructure of an as-quenched Al-3Li-2Be alloy. The prominent features of this structure are indicated on the micrographs, and include coherent  $\text{Al}_3\text{Li}$   $\delta'$  precipitates (A), Be-rich particles (B); some regions of cellular structure are also observed. This nonuniform microstructure is similar to that of splat-quenched Al-Be alloys. The  $\delta'$  particles are approximately 5-10 nm in diameter, which is considerably finer than  $\delta'$  observed in Al-Li base alloys produced by powder or ingot techniques. The volume fraction of large (>100 nm) Be-rich particles is relatively low (<10%) and these particles are usually confined to grain boundary regions.

The striking feature evident in the micrographs in Figure 17(b) is the segregated cellular structure of the as-quenched Al-3Li-10Be ribbon. There is an enrichment of small Be-rich particles concentrated at the cell walls. Although it is not obvious from this figure, the volume fraction of large Be-rich particles is greater in the Al-3Li-10Be alloy than in the Al-3Li-2Be alloy. The inserted [001] zone axis pattern clearly shows the [100]-type reflections from  $\delta'$  (identical patterns were obtained from Al-3Li-2Be). These precipitates have the typical cube-cube orientation relationship with the matrix (i.e.,  $[100]\delta'/[100]\text{Al}$ ,  $(001)\delta'/(001)\text{Al}$ ).

The selected-area diffraction technique was not sensitive enough to reveal the crystal structure of the Be-rich particles; therefore, microdiffraction tech-

Of particular interest are the regions observed in these photomicrographs that are apparently devoid of the  $\delta'$  precipitate. The  $\alpha$ -Be particles can be observed on the high angle boundary on the right hand side of the photomicrographs. A region from within Figure 13 is shown at high magnification in Figure 14. In this case the many  $\alpha$ -Be particles within the cell walls are clearly visible. Within the cells, larger  $\alpha$ -Be particles and occasional dislocation loops are found. A region from the boundary between a cell wall and the interior is shown in Figure 15. In addition to the large  $\alpha$ -Be particle in the cell interior and fine  $\alpha$ -Be particles in the cell wall, the individual  $\delta'$  particles can be resolved in the matrix and there is some evidence of streaking (left hand side) associated with them.

### 3.4 Melt Spun Al-Li-Be Alloys

Two of the alloys (Al-3Li-2Be and Al-3Li-10Be) were converted to melt spun ribbon using equipment designed and built at the Lockheed Palo Alto Research Laboratory<sup>(9)</sup>. Ribbon of approximate dimensions 1 mm in width and less than 0.1 mm thickness was produced and examined using optical and transmission microscopy.

Optical photomicrographs of melt spun ribbon of the Al-3Li-10Be alloy are shown in Figure 16. As may be seen, relatively uniform fine microstructures were observed using optical microscopy. These fine structures can be compared with those produced by splat quenching of the same alloy (Figure 9) and it is evident that the melt spinning operation produces a more uniform, finer structure than does the splat quenching.

In order to examine the structures of the ribbons more closely, a TEM examina-

tion of the  $\delta'$  particles is sufficiently uniform that, as expected, there was no evidence to suggest that this precipitation defined the cell or grain size.

The  $\alpha$ -Be particle volume fraction is quantitatively observed to follow the expected trend, i.e., the volume fraction in the Al-3Li-10Be sample was greater than that in the Al-3Li-2Be sample. In both cases the  $\alpha$ -Be particles were less than 100 nm in size and generally in the range from 5 to 50 nm. The smaller particles were usually confined to cell boundaries or grain boundaries. The large particles (100 nm) were randomly dispersed throughout the alloys. As may have been anticipated from the optical metallographic results, the microstructure was observed to be somewhat nonuniform even within a particular sample. For example, a given grain would be observed to contain a larger volume fraction of  $\alpha$ -Be than an adjacent grain. This would be an expected consequence of nonuniformities in both liquid and solid quench rates. Details of these microstructures are presented below for splat-quenched Al-3Li-2Be and Al-3Li-10Be alloys.

An area from the splat quenched Al-3Li-2Be alloy is shown in Figure 10 and the cellular structure described above is observed. The dislocation density within cells varied considerably as may be seen (high density in the top left of Figure 10). The  $\delta'$  particle distribution is shown in the dark field photomicrograph of Figure 11 using a  $\delta'$  reflection. A high magnification bright field view from a region within Figure 11 is shown in Figure 12. In both these figures there is evidence of small denuded zones (of  $\delta'$ ) adjacent to both low angle boundaries and high angle boundaries.

A bright field/weak beam dark field pair of photomicrographs in Figure 13 illustrates the distribution of  $\delta'$  in the Al-3Li-10Be splat quenched alloy.

exercised in selecting portions for splat alloy preparation or additional precautions must be taken to assure homogeneity.

Table 1 also shows compositional information obtained from light and dark microscopic phases present in the sample. These data, 1(a) through (c), obtained from the general area 1, indicate that little or no variation in Li concentration occurs in thin microscopic regions. On the other hand, the Al/Be ratio varied substantially suggesting precipitation of Be-rich and Be-deficient phases within this region.

### 3.3 Splat Quenched Al-Li-Be Alloys

Three of the Al-Li-Be alloys were prepared by splat quenching. A typical splat quenched sample is shown in Figure 8. The splat technique results in a nonuniform thickness from the center to the edge of the splat and, as a result, the microstructure varies considerably within a given splat. This is illustrated in Figure 8 for the Al-3Li-10Be alloy. Nonetheless, it is possible to compare the microstructures of the three alloys and this comparison is shown in Figure 9. As may be seen, the incidence of primary Be particles is evident at the high Be concentrations even in these samples produced by splat quenching.

A transmission electron microscopy study was carried out on material cut from splat quenched Al-3Li-2Be and Al-3Li-10Be alloys. It was observed that alloys from both compositions contained mainly cellular microstructures. The cell walls were defined by dislocations and were associated with  $\alpha$ -Be particles. In general, the  $\delta'$  particles were uniformly distributed; some rather unusual exceptions were observed, however, and these will be discussed. The distribu-

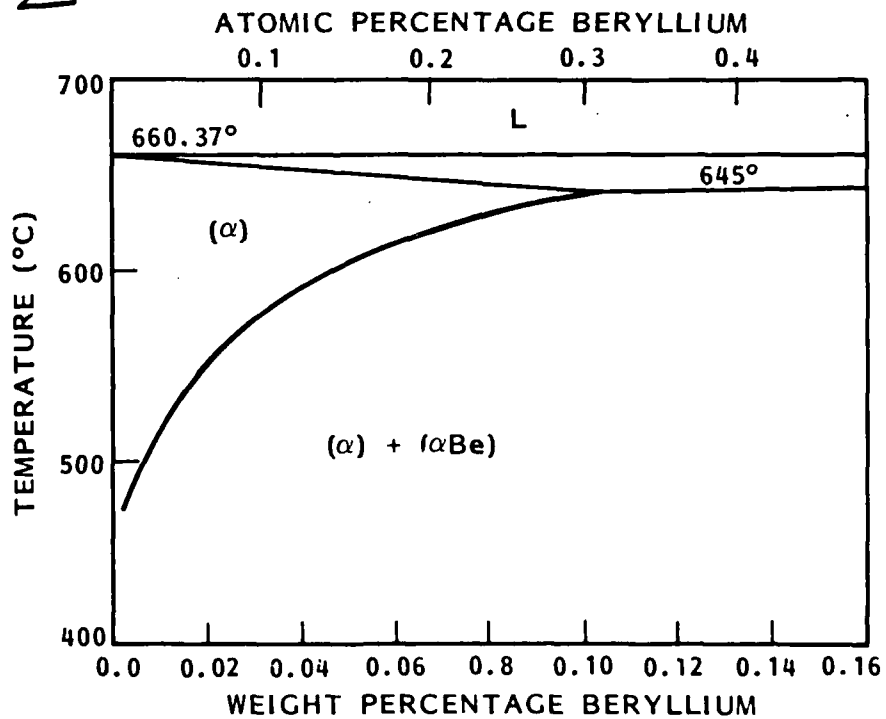
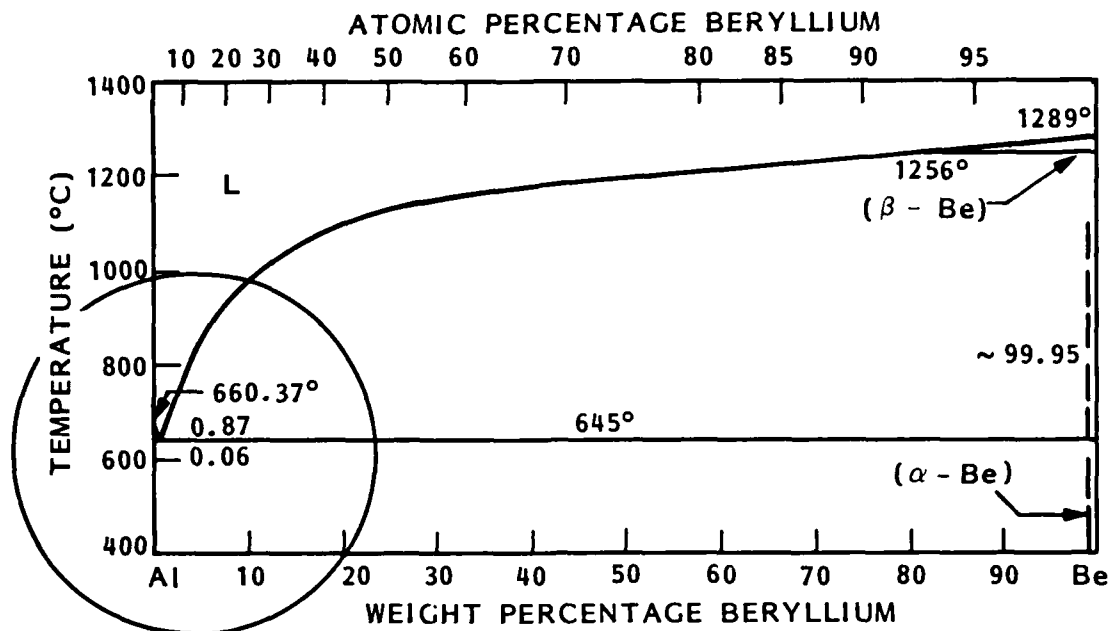


Figure 1 The Aluminum-Beryllium phase diagram.

AL-Li-Be ALLOYS

ARC MELTED + ACID ETCHED

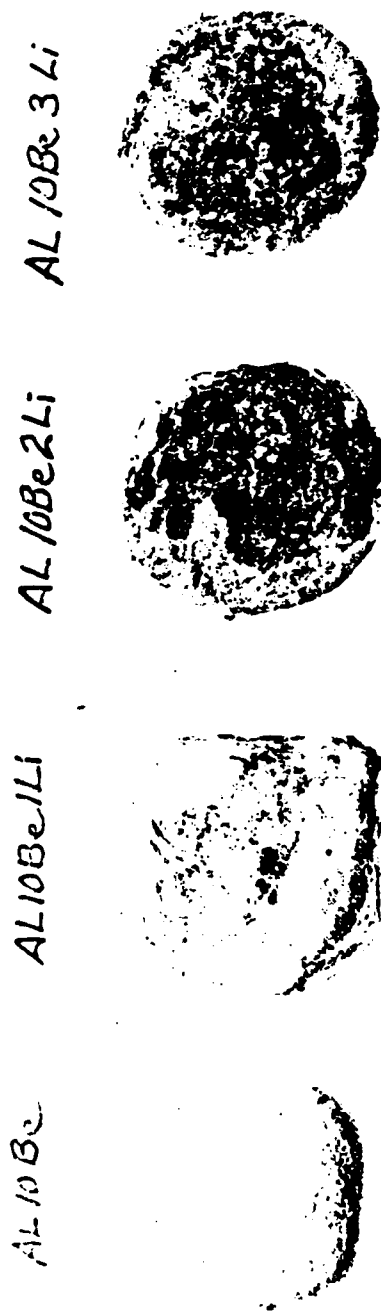
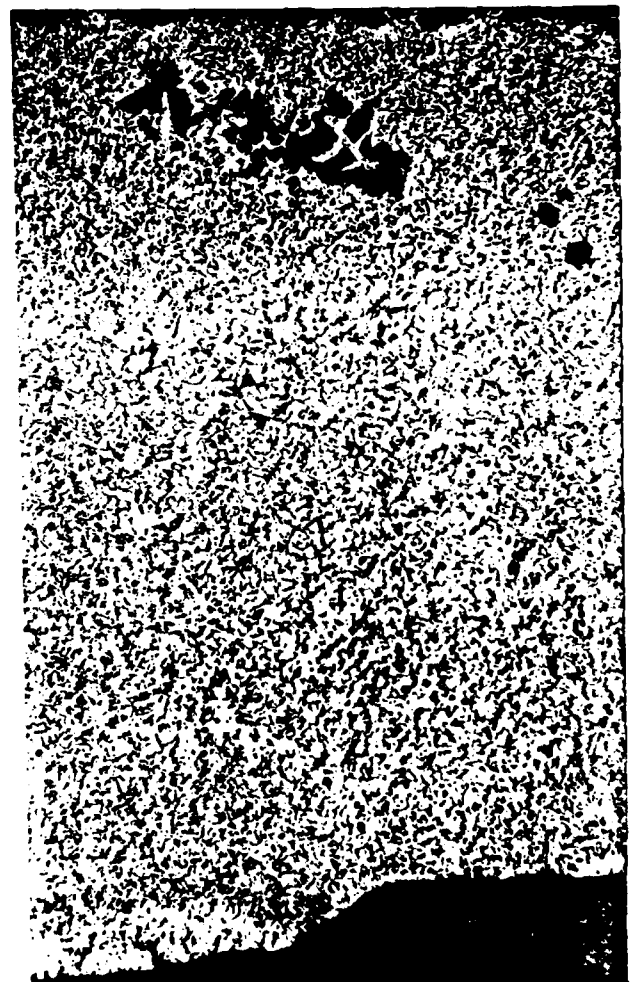
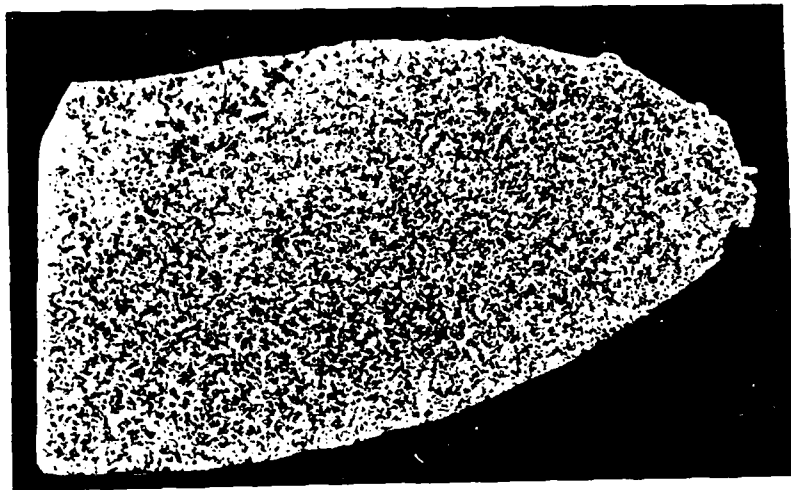


Figure 2 Arc-melted castings of Al-Li, Al-Be and Al-Li-Be alloys.



2 mm

Figure 3 Sections of the arc-melted castings of Al-3Li-2Be (top) and Al-3Li-10Be (bottom pair) alloys.

4a

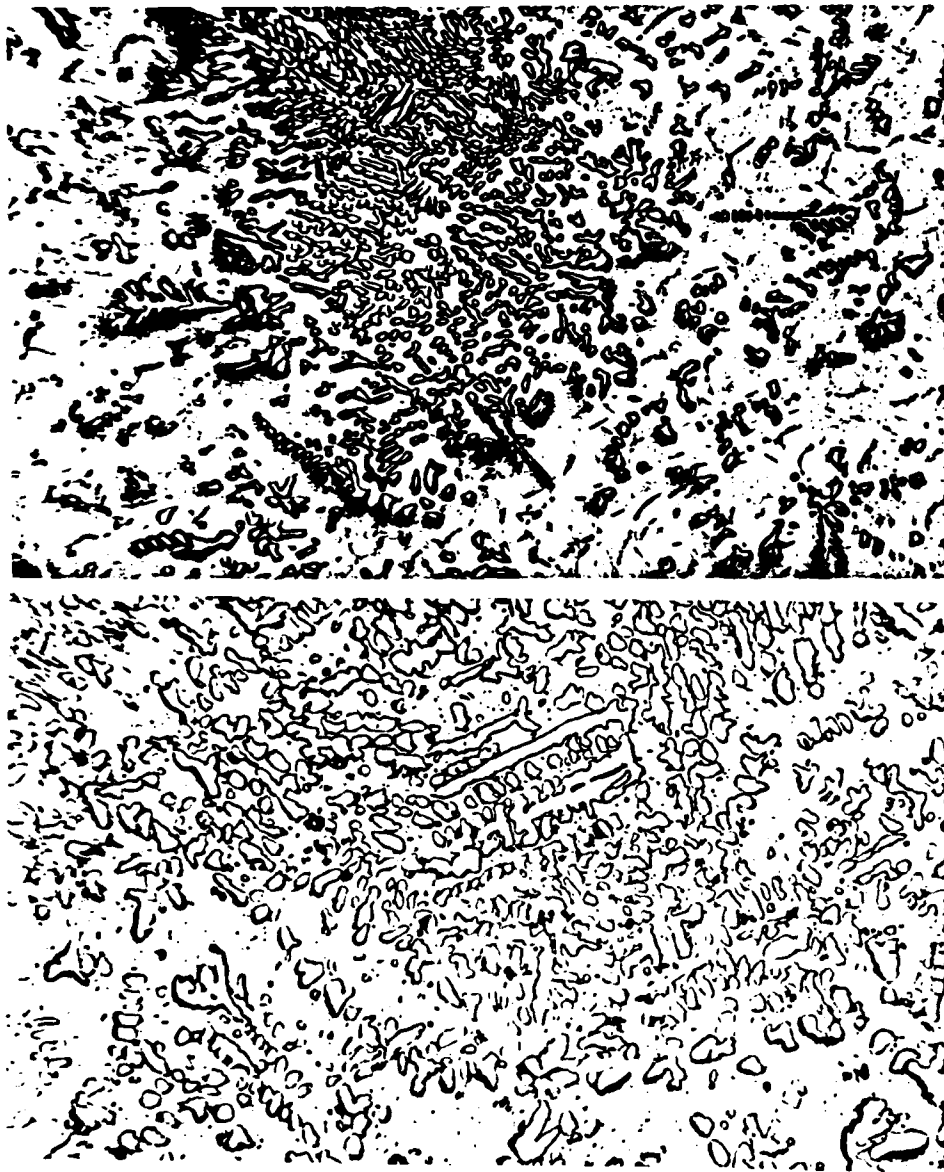
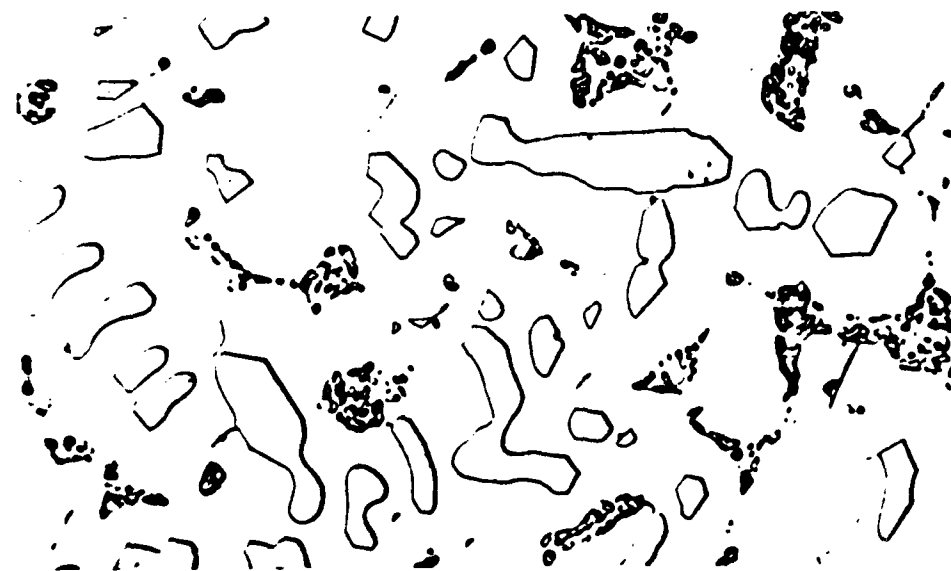
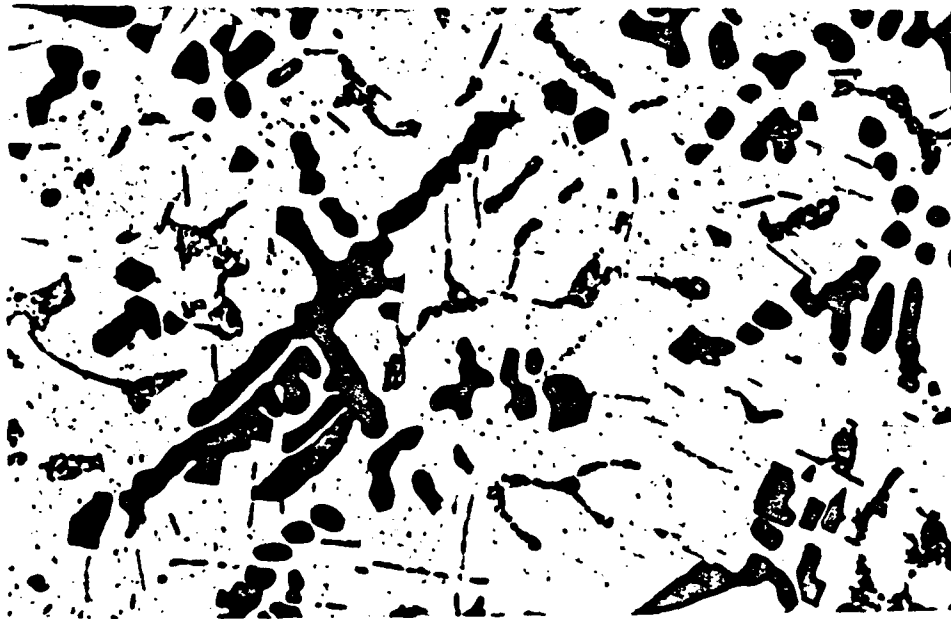


Figure 4 Optical photomicrographs at (a) low, (b) medium, and (c) high magnification for the Al-3Li-2Be (top), Al-3Li-5Be (medium) and Al-3Li-10Be (bottom) alloys in the arc melted condition.

4b



4c

10  $\mu$ m



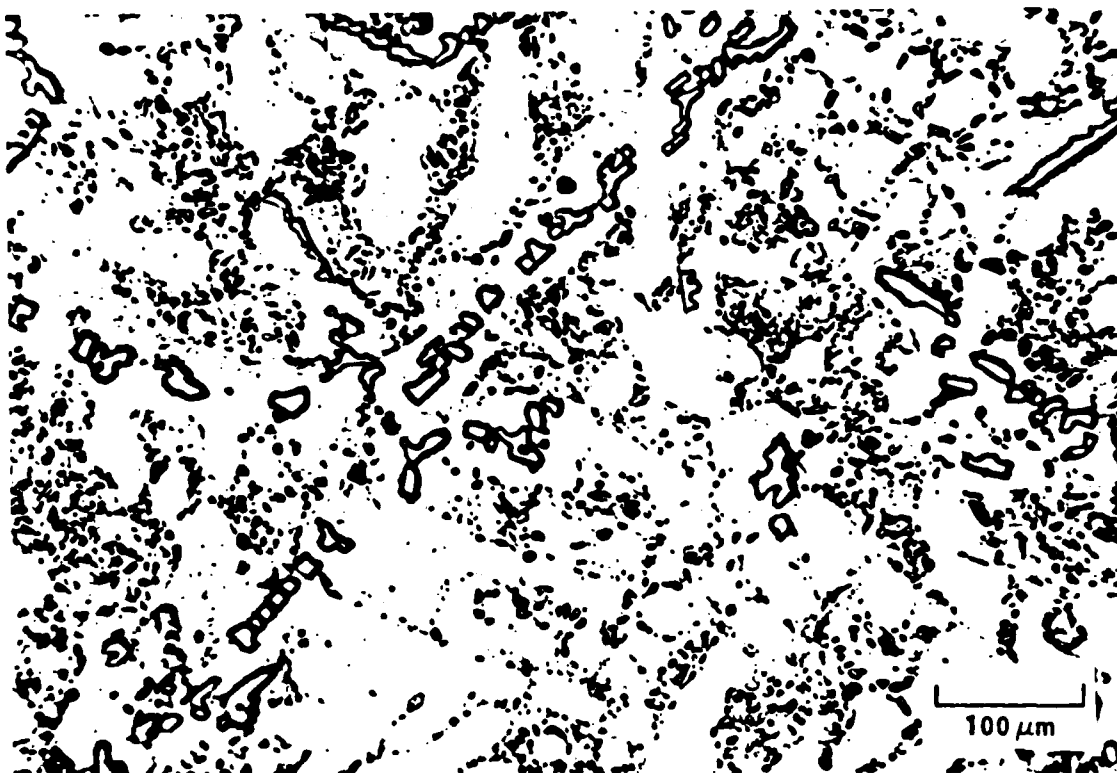
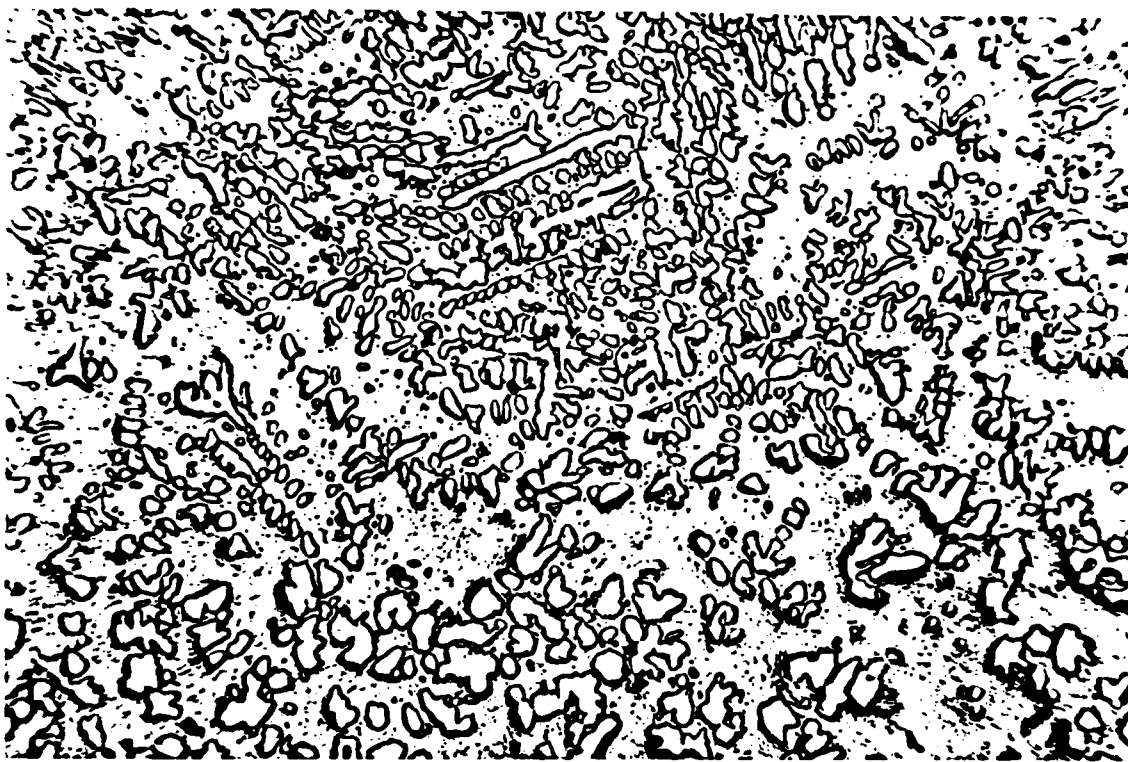


Figure 5 Variations of microstructure within the arc melted Al-3Li-10Be alloy.

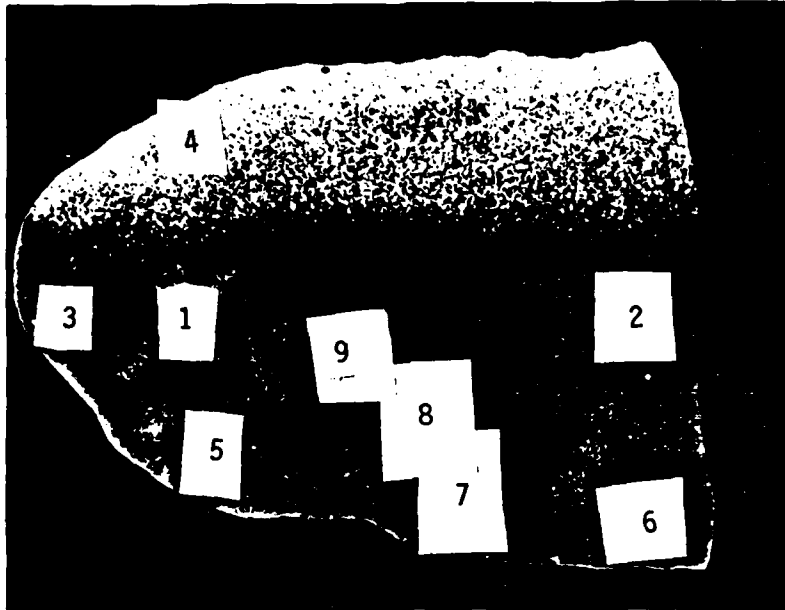


Figure 6 Cast slice of Al-3Li-10Be alloy showing the areas studied by Auger analysis.

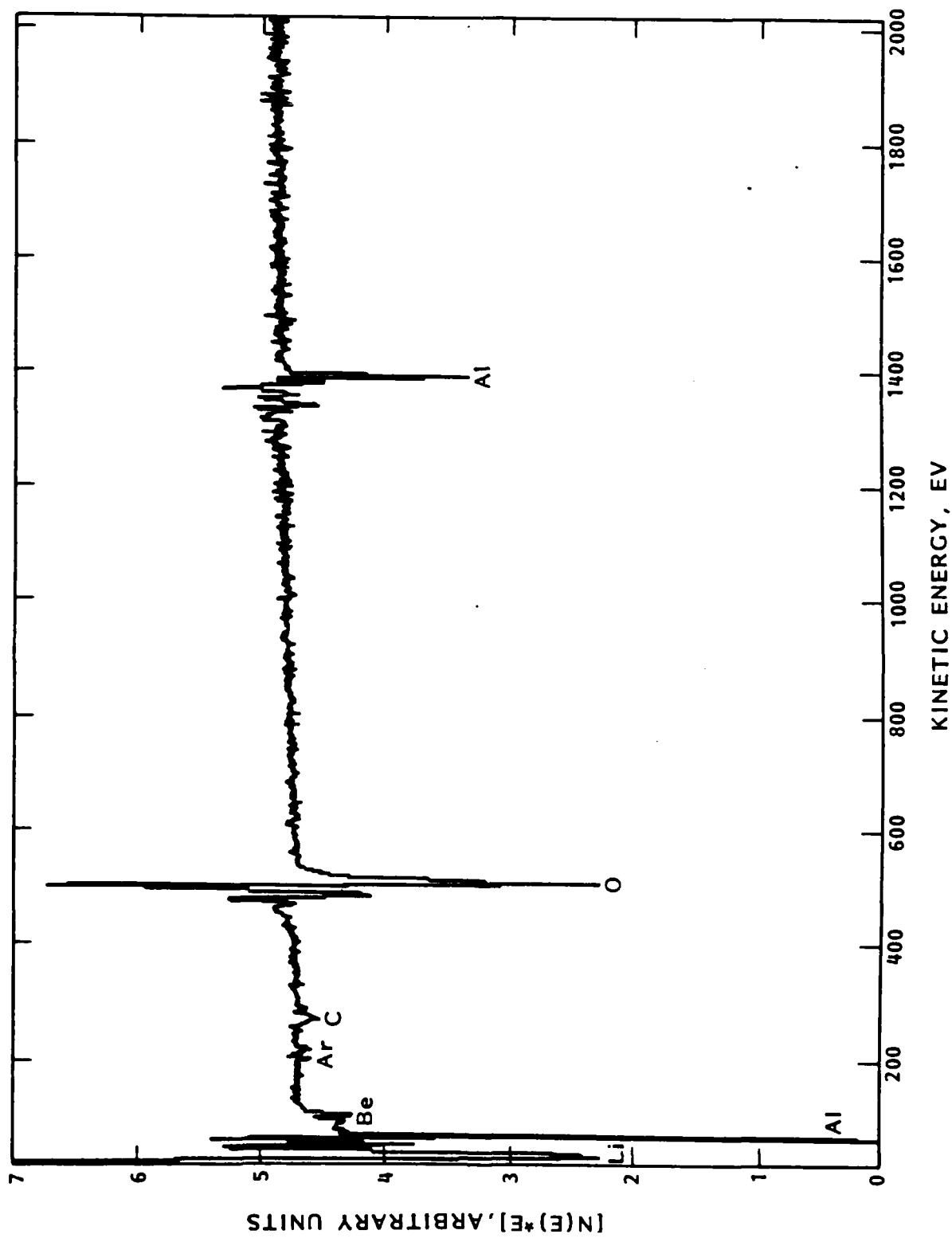
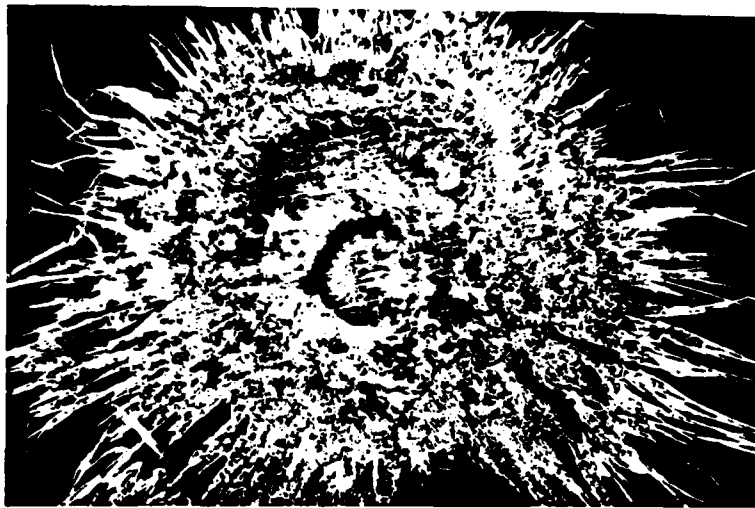
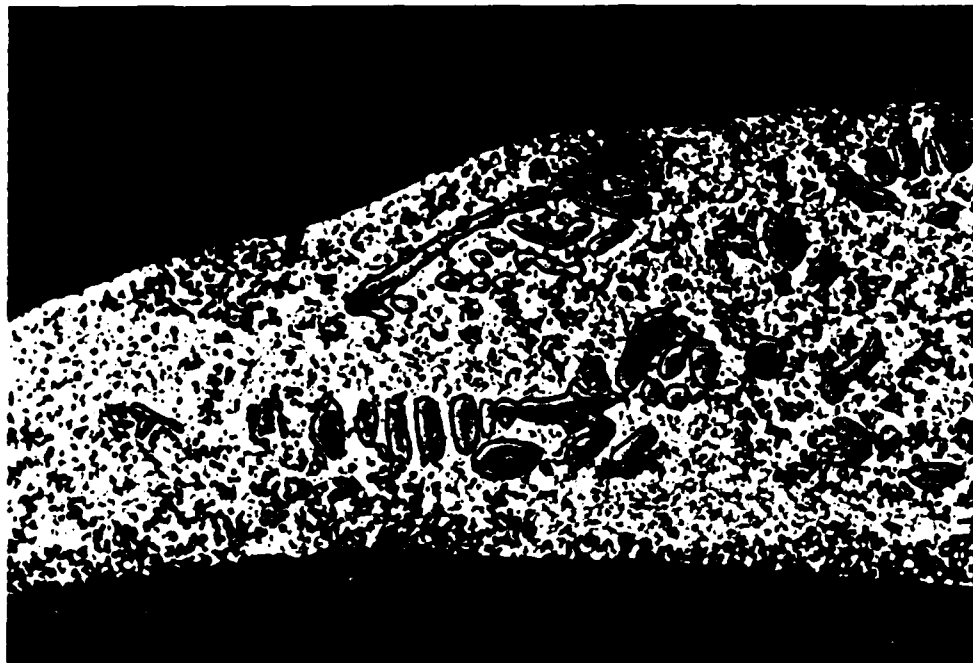


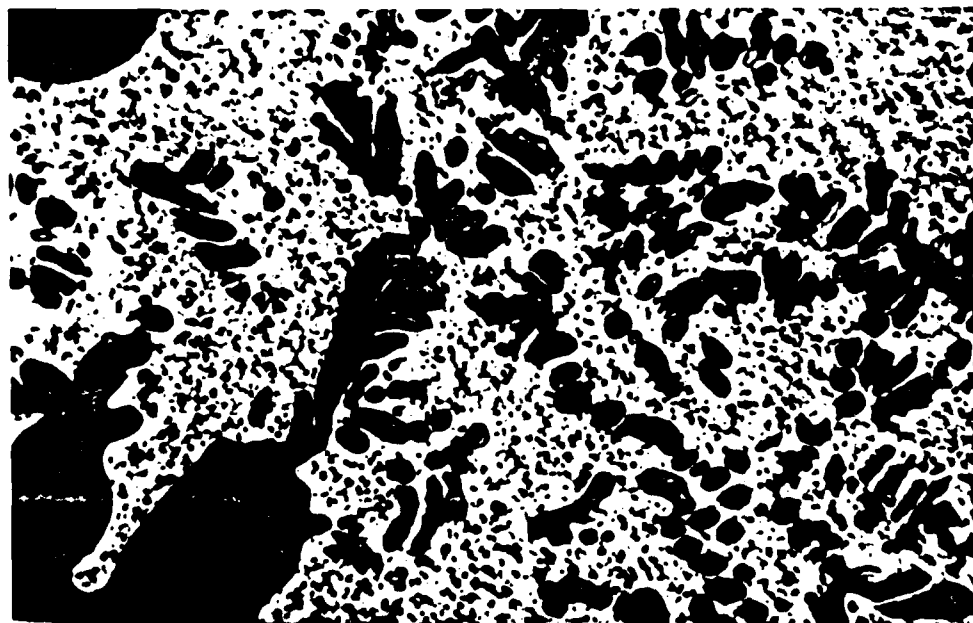
Fig. 7 AES spectrum from area 4 of Figure 6.



5 mm

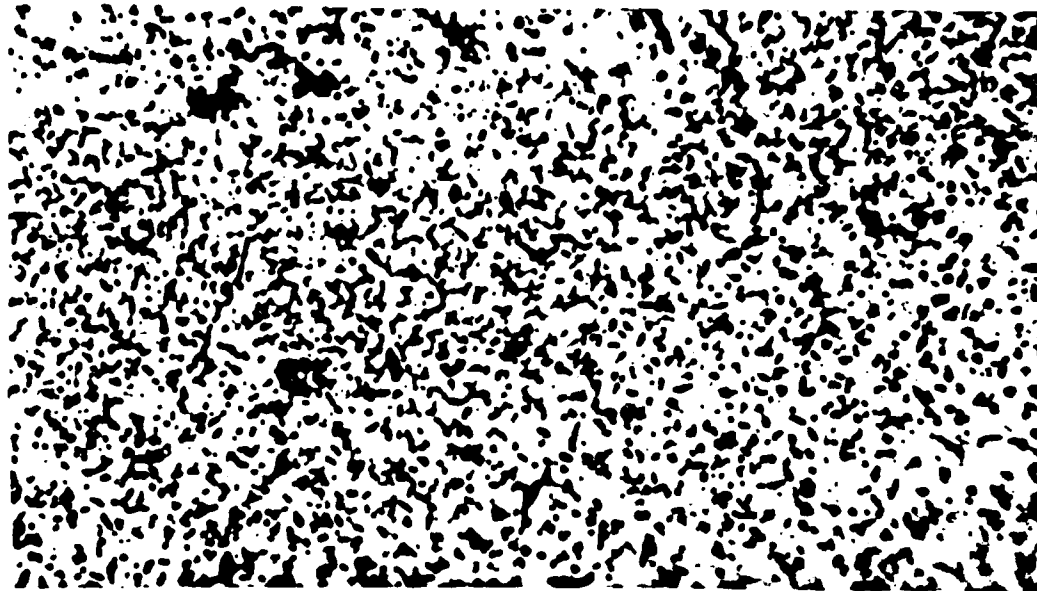


20  $\mu\text{m}$



10  $\mu\text{m}$

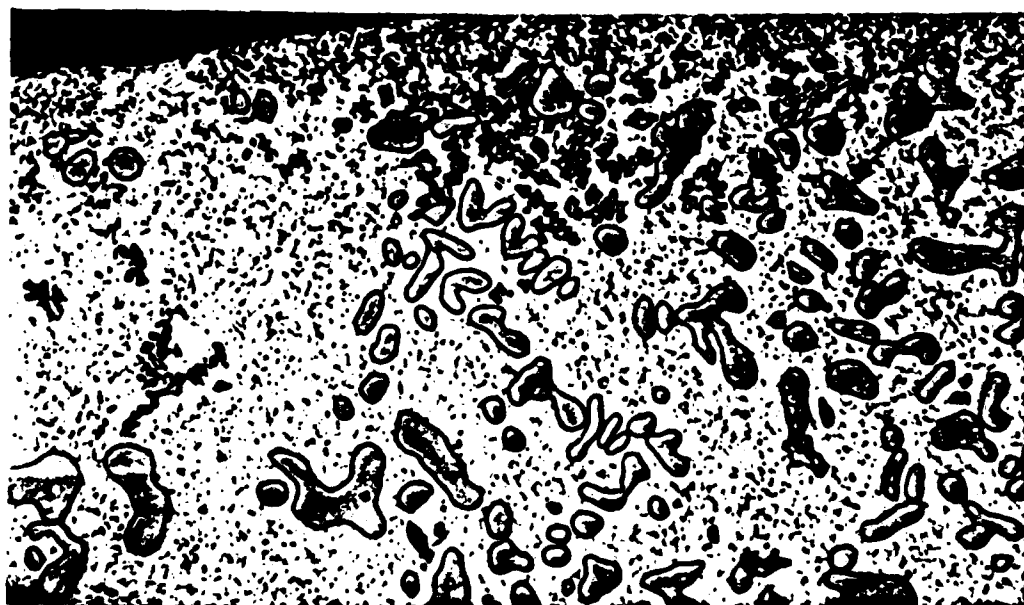
Figure 8 (a) Splat quenched sample.  
(b) Profile through splat quenched sample.  
(c) Microstructural variation within a splat quenched Al-3Li-10Be alloy.



10  $\mu\text{m}$



10  $\mu\text{m}$



20  $\mu\text{m}$

Figure 9 Microstructures of the splat quenched Al-3Li-2Be (top), Al-3Li-5Re (center), and Al-3Li-10Be (bottom) alloys.



Figure 10 Transmission electron micrograph of the cellular structure observed within an Al-3Li-2Be splat quenched sample.

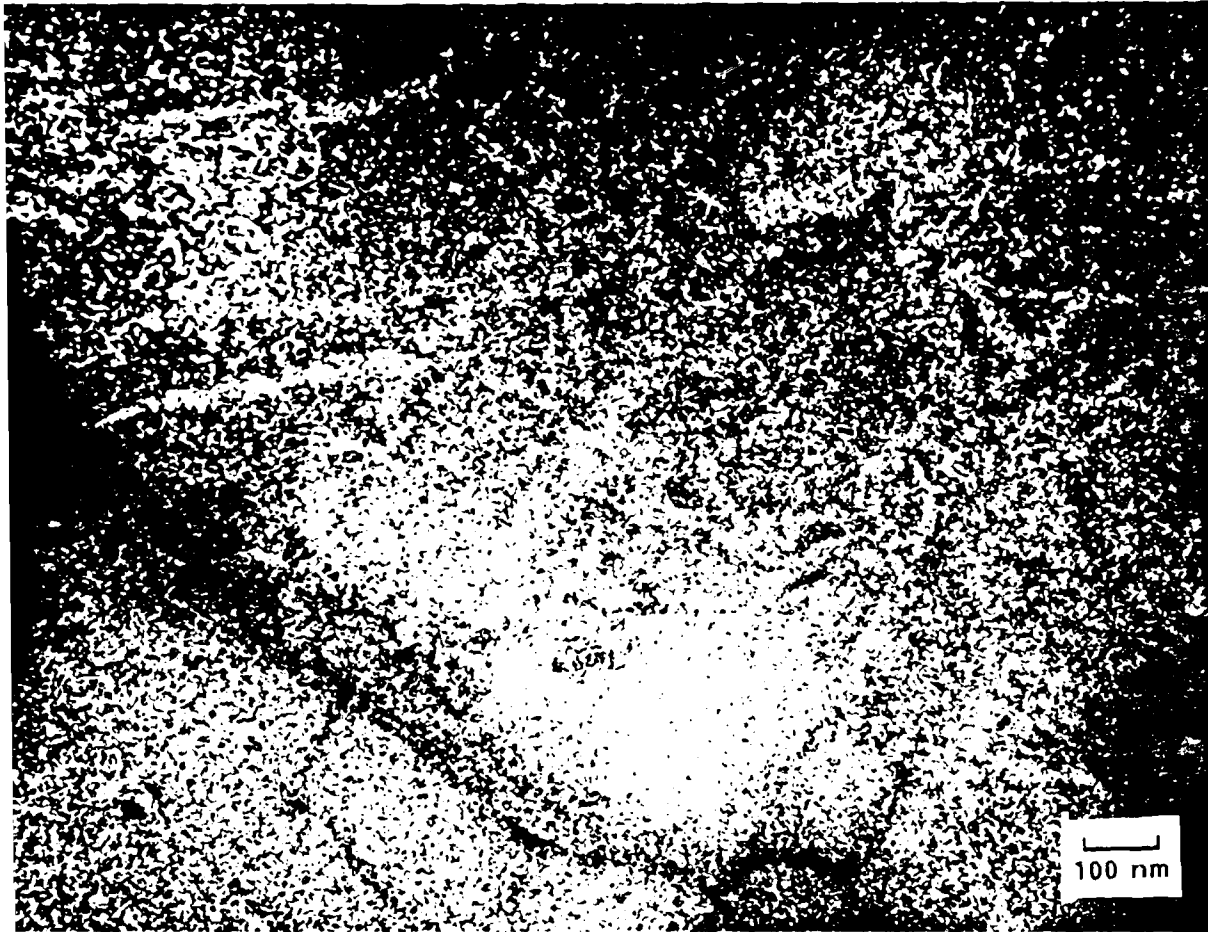


Figure 11 TEM of the  $\delta'$  particle distribution using a dark field technique in the Al-3Li-2Be splat quenched sample.



Figure 12 High magnification (bright field) of a region within Figure 11 of an Al-3Be-2Be splat quenched sample.



Figure 26 Al-3Li-10Be consolidated alloy in the T6 condition after testing testing.

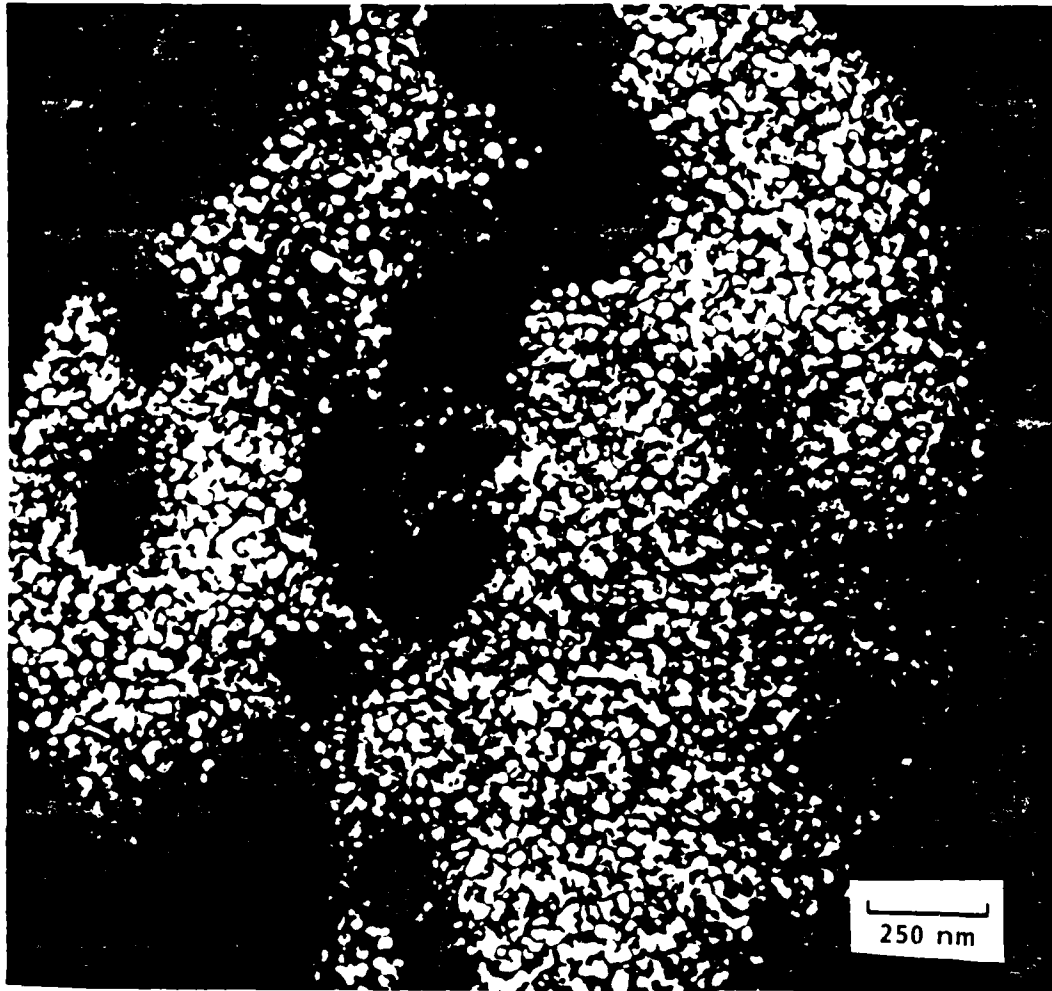


Figure 25 BF/WBDF pair showing depleted region of  $\delta'$  adjacent to grain boundaries and depleted regions within the grains of tensile tested Al-3Li-2Be alloy.



Figure 24 Consolidated Al-3Li-2Be after tensile testing.



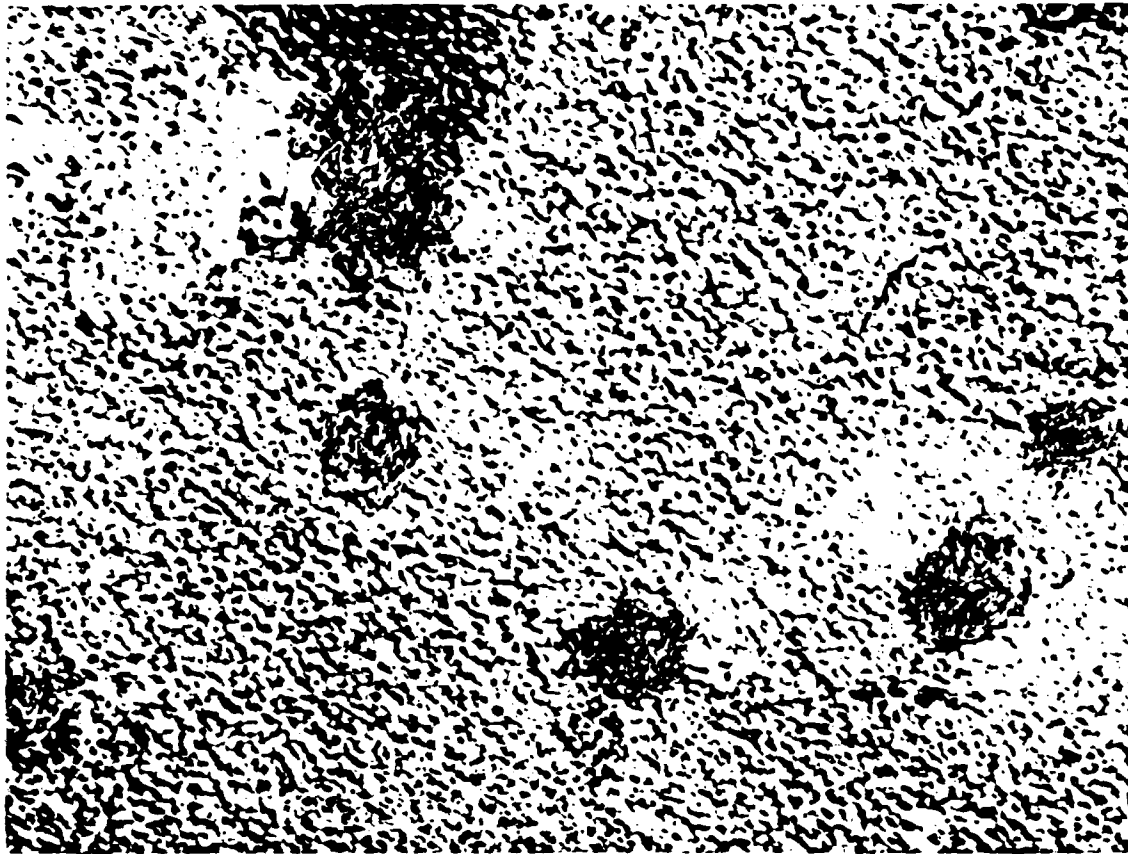
Figure 23 Region from within Figure 22 showing agglomeration of small Be particles as a result of consolidation.



Figure 22 Consolidated and heat treated Al-3Li-10Be alloy.



Figure 21 TEM collage of the Al-3Li-10Be consolidated melt-spun ribbon in the extruded plus T6 heat treatment condition.



250 nm

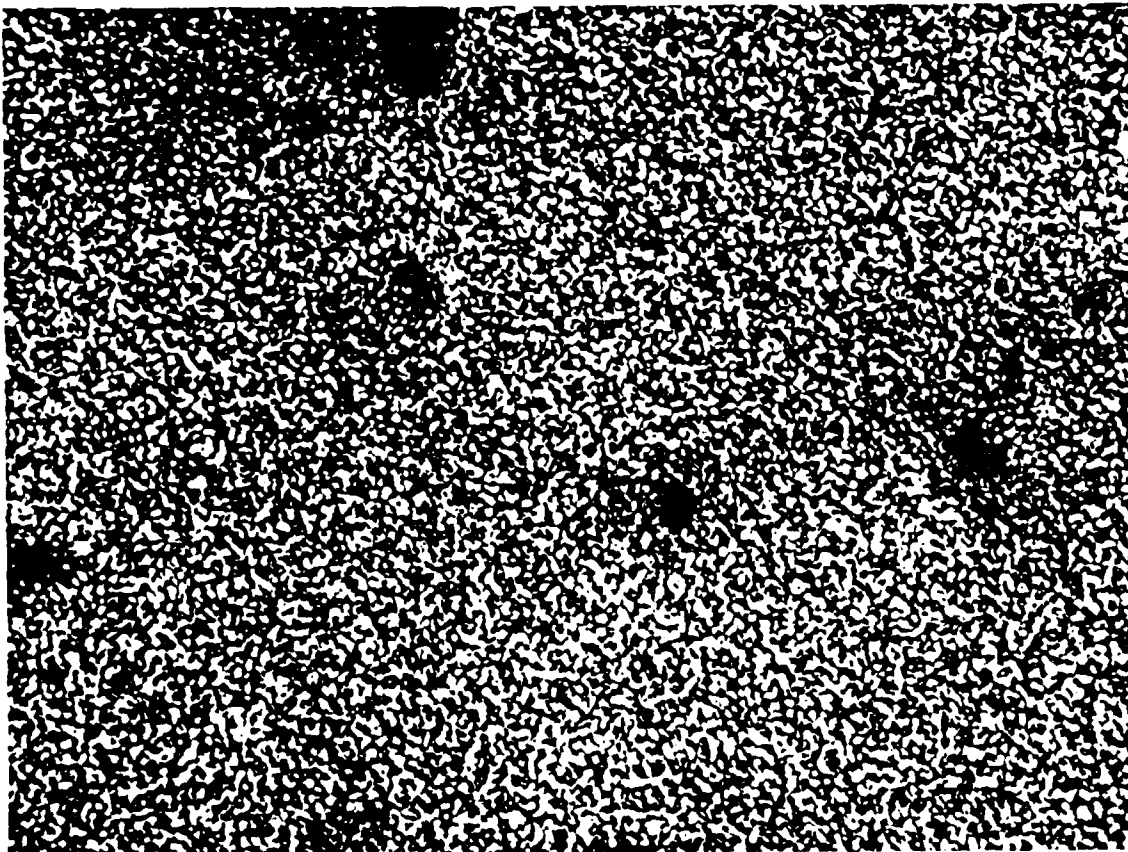


Figure 20 BF/WBDF ( $\delta'$  reflection) pair of TEMs from the Al-3Li-2Be consolidated ribbon in the extruded and heat treated to T6 condition

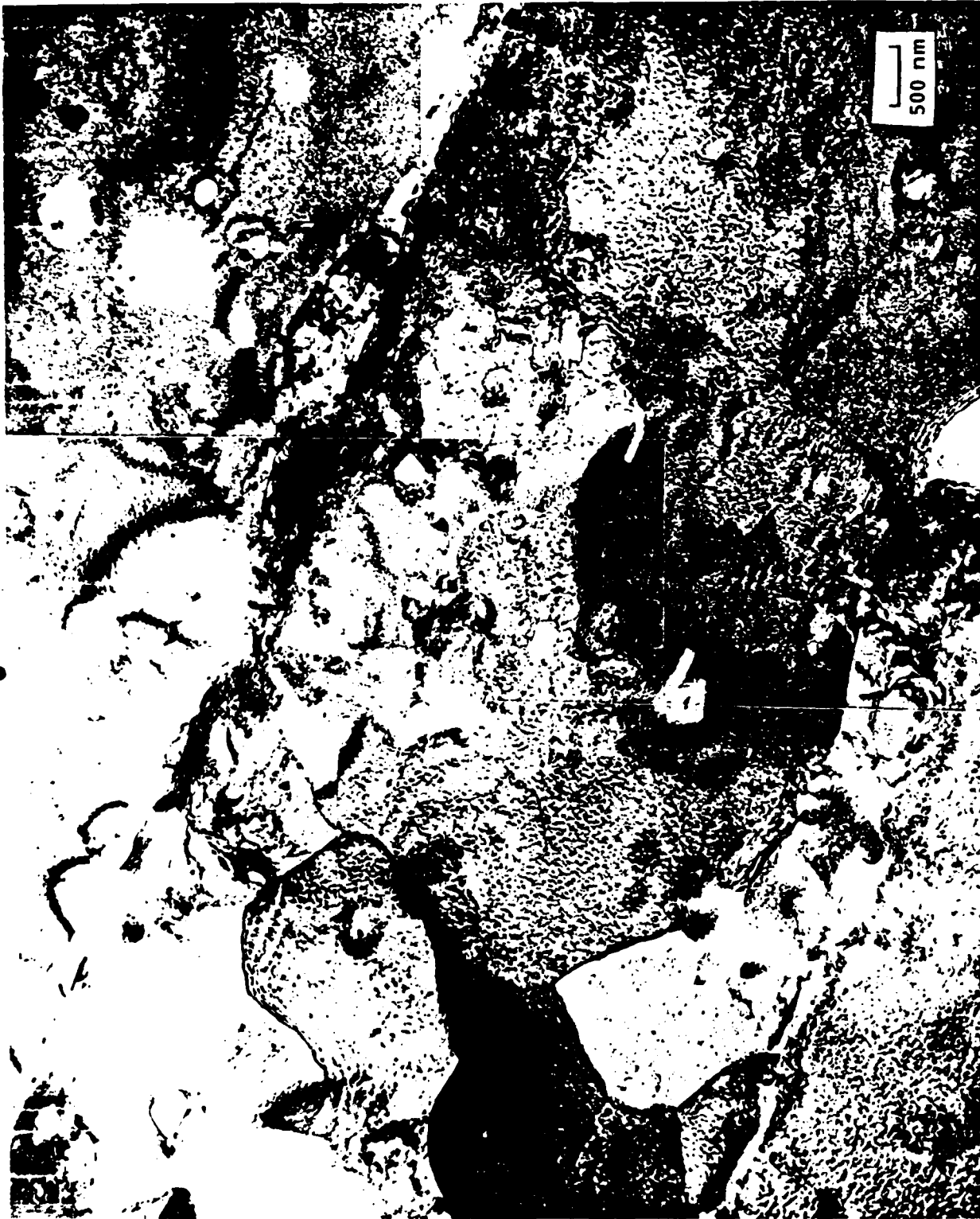


Figure 19 Consolidated ribbon of Al-3Li-2Be alloy, extruded and heat treated to the T6 condition, but from a nearby region to that in Figure 18. In this case, elongated grains and subgrains are observed in addition to  $\alpha$ -Be particles and deformation zones.

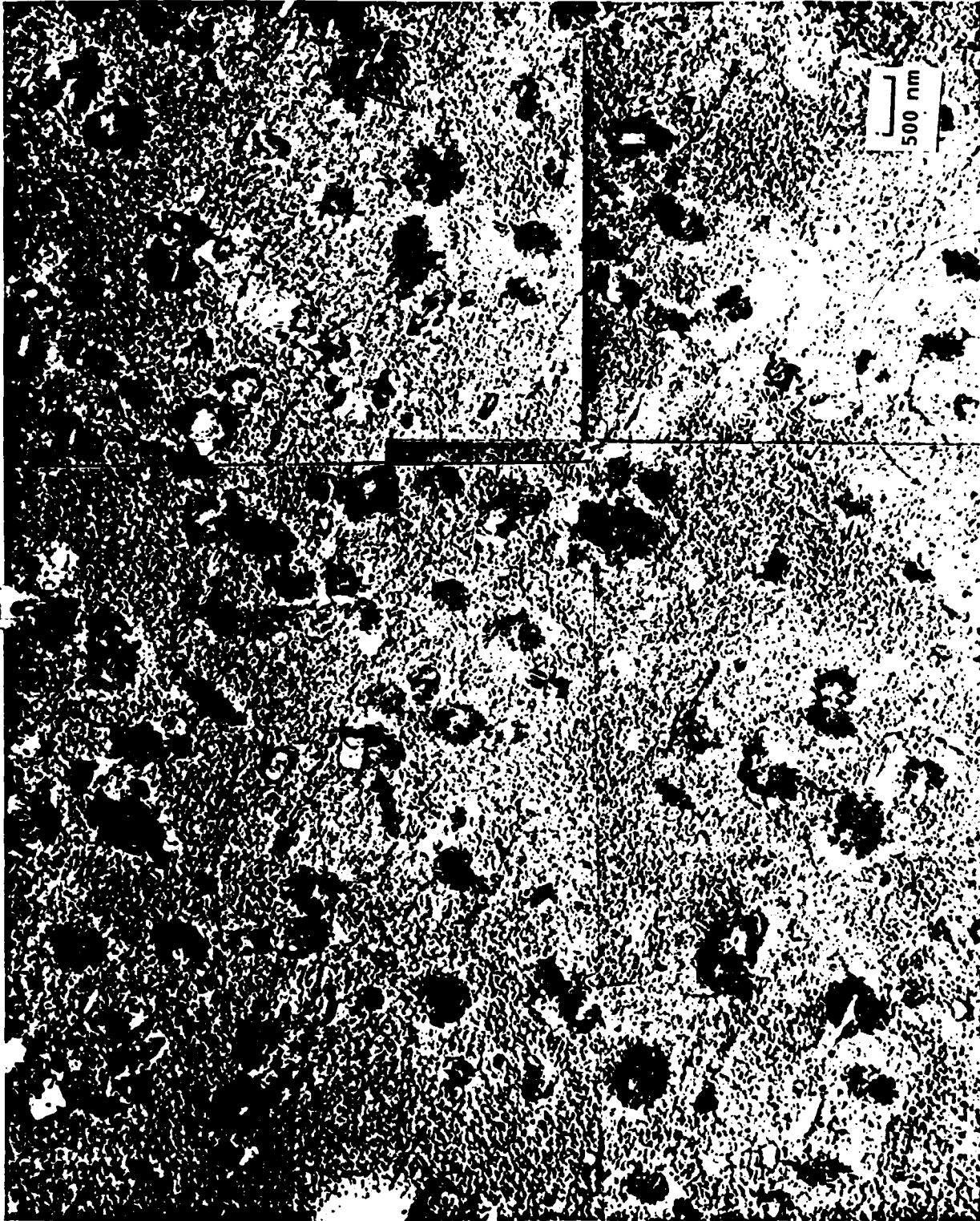


Figure 18 Consolidated ribbon of Al-3Li-2Be alloy, extruded and heat treated to the T6 condition. This region shows a single crystal containing  $\alpha$ -Be particles associated with intense deformation zones.

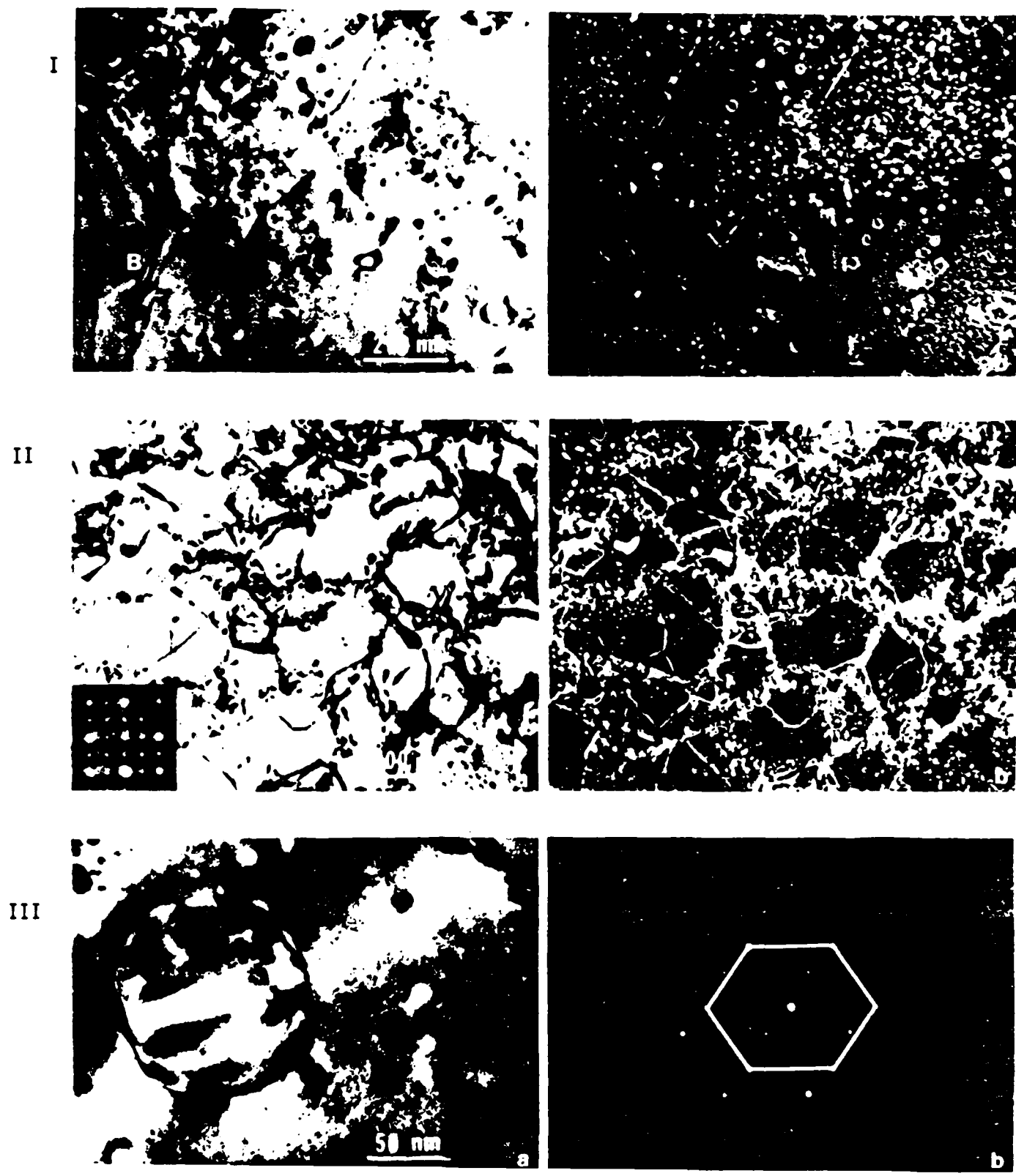


Figure 17 I. (a) Bright field and (b) weak-beam dark field of Al-3Li-2Be ribbon.  
 II. (a) Bright field and (b) weak beam dark field of Al-3Li-10Be ribbon with inserted [001] diffraction pattern showing  $\delta'$  reflection.  
 III. (a) Bright field and (b) microdiffraction pattern of Be-rich particle in Al-3Li-10Be ribbon.



Figure 16 Optical photomicrographs of the melt-spun Al-3Li-10Be alloy (contact surface is the lower surface in each case) at low (top) and high (bottom) magnifications in the etched condition.

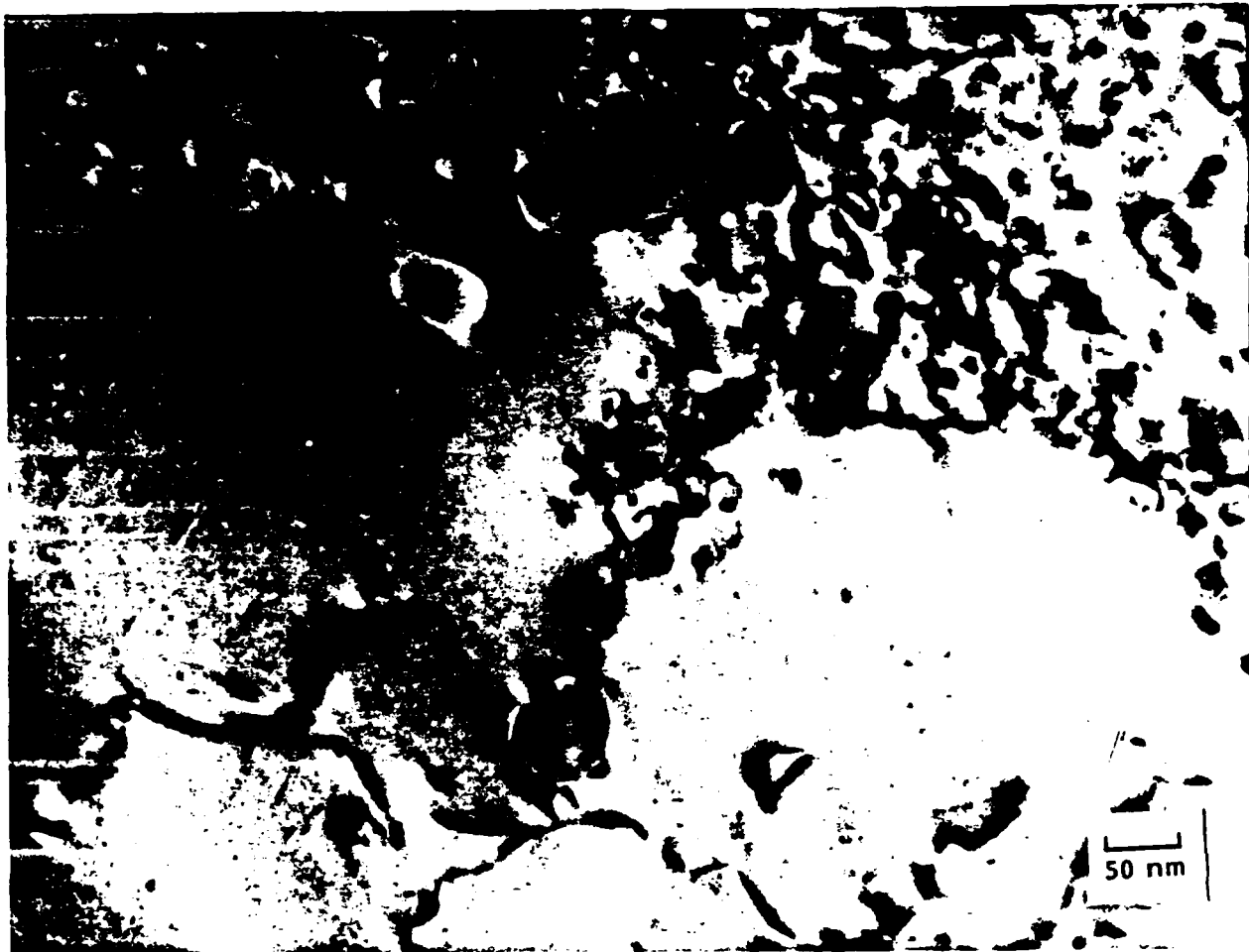


Figure 15 High magnification TEM of the splat quenched Al-3Li-10Be alloy showing the boundary region at a cell wall.

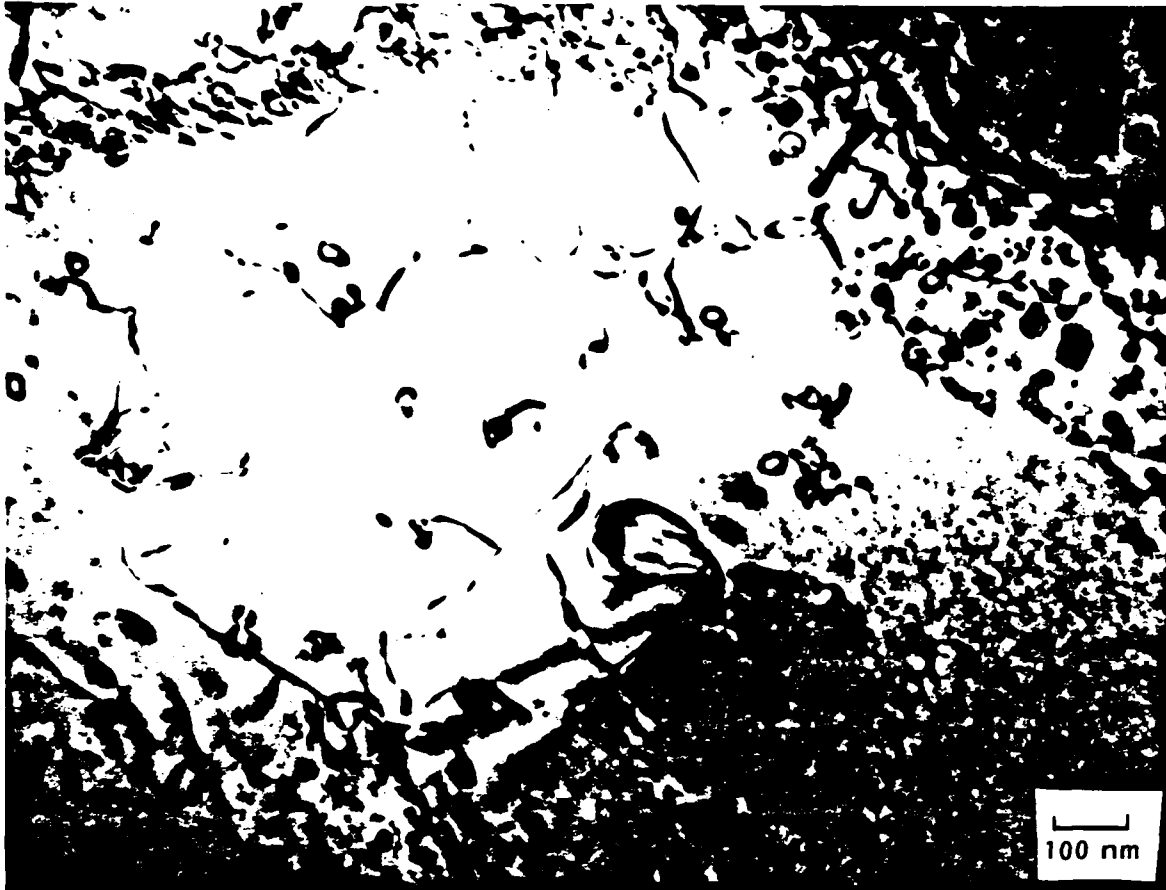
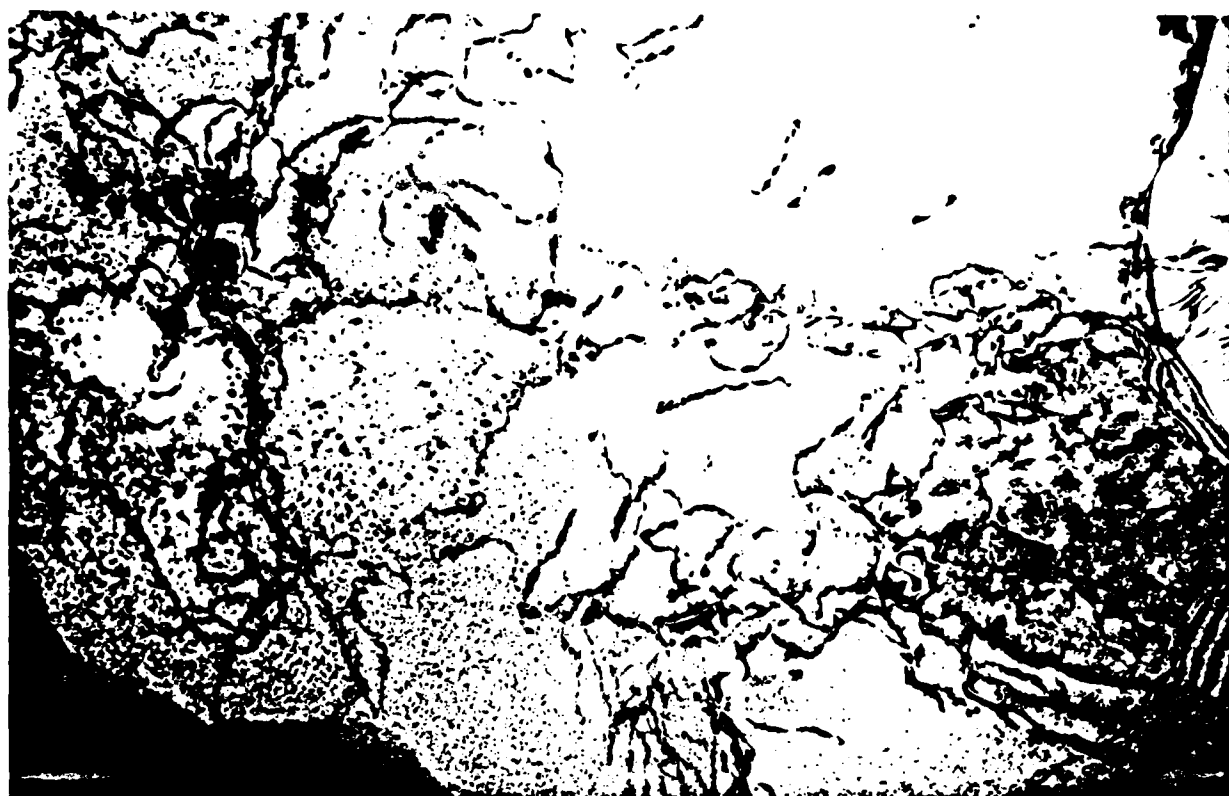


Figure 14 TEM OF Al-3Li-10Be splat quenched alloy showing the  $\alpha$ -Be particles predominantly at cell walls.



250 nm

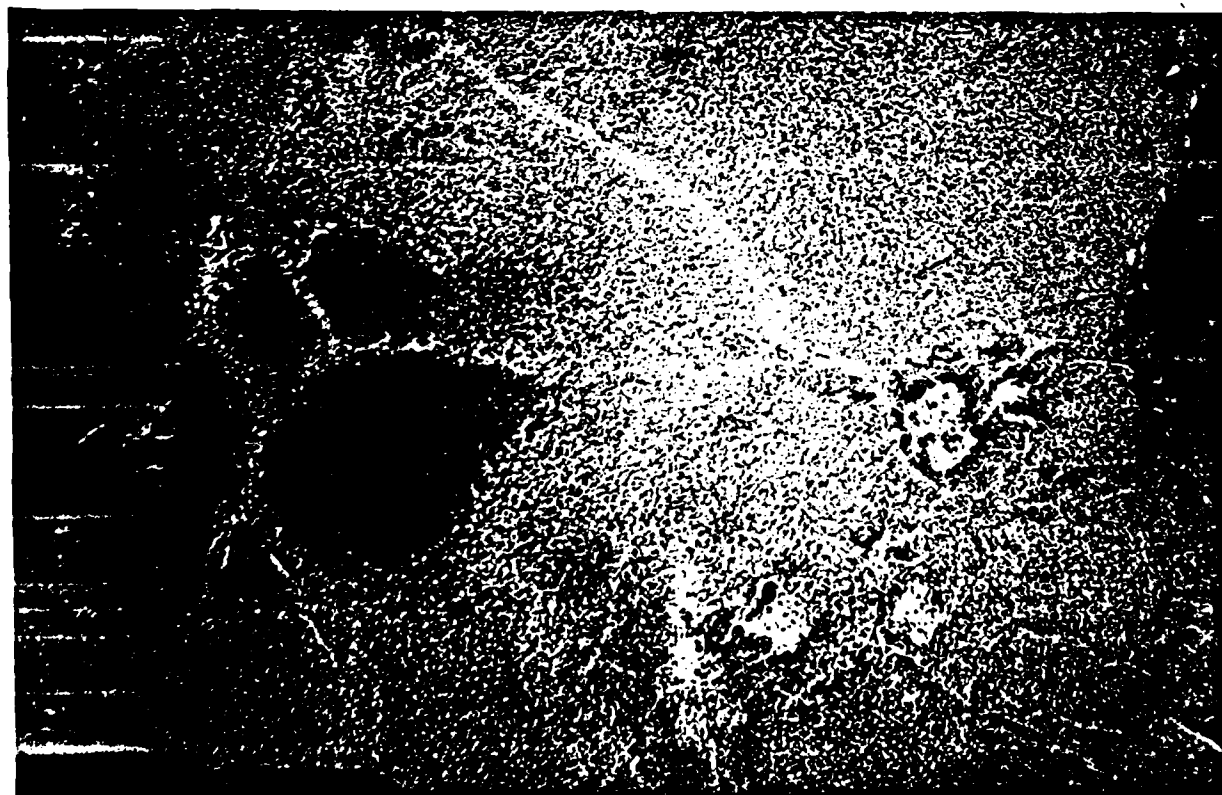


Figure 13 Bright field/weak beam dark field pair of TEMS illustrating the distribution of  $\delta'$  within the Al-3Li-20Be splat quenched alloy.



100 nm

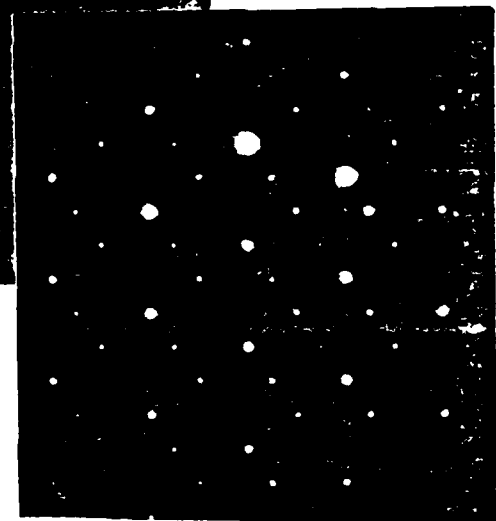
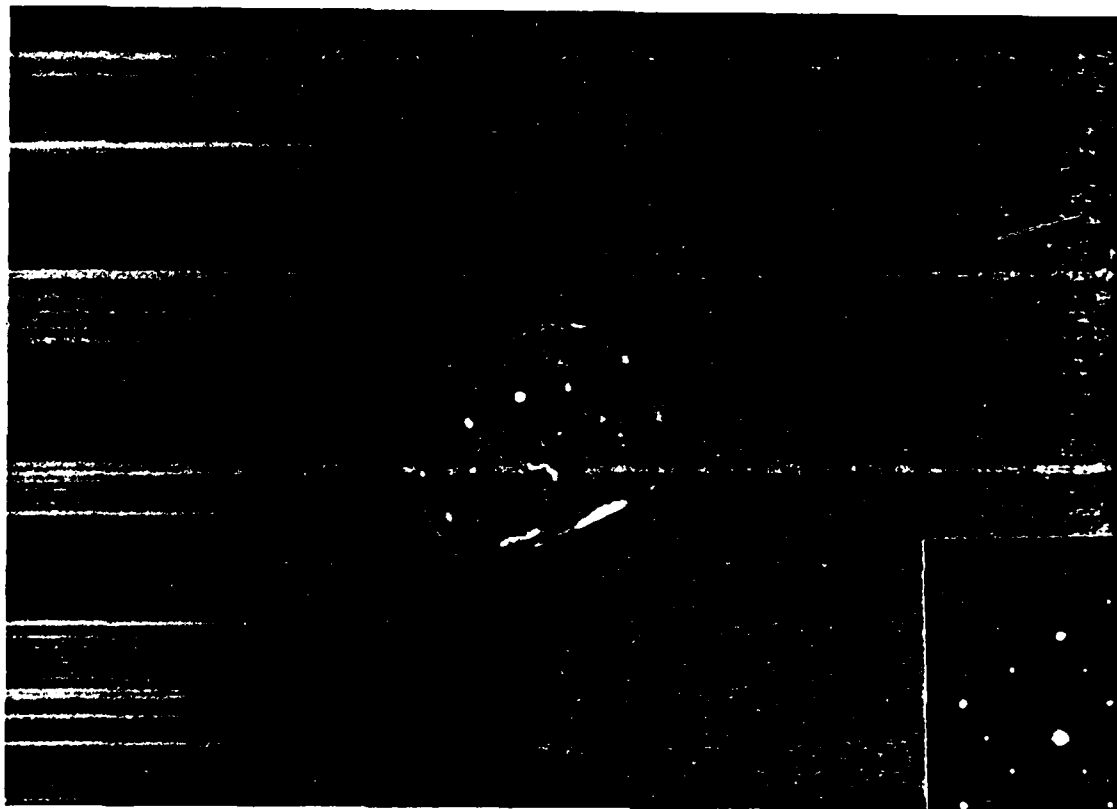


Figure 27 BF/WBDF TEM pair showing small Be particles on an  $\alpha$ -Be particle in the Al-3Li-10Be consolidated alloy. The convergent beam electron diffraction pattern is typical for this type of precipitation.

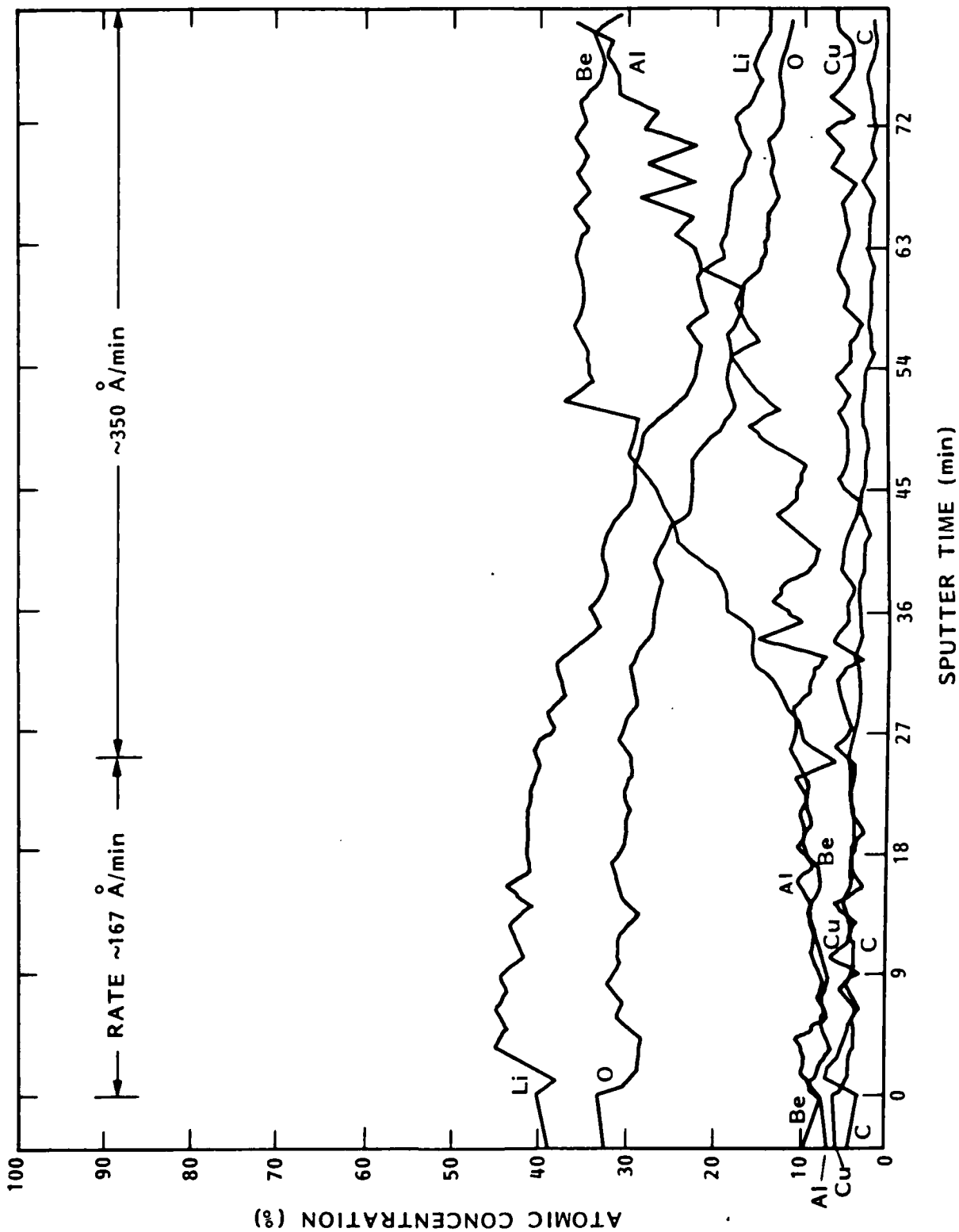


Fig. 28 AES depth profile of Al-10wt%Be-3wt%Li ribbon in as-spun condition, roll facing surface.

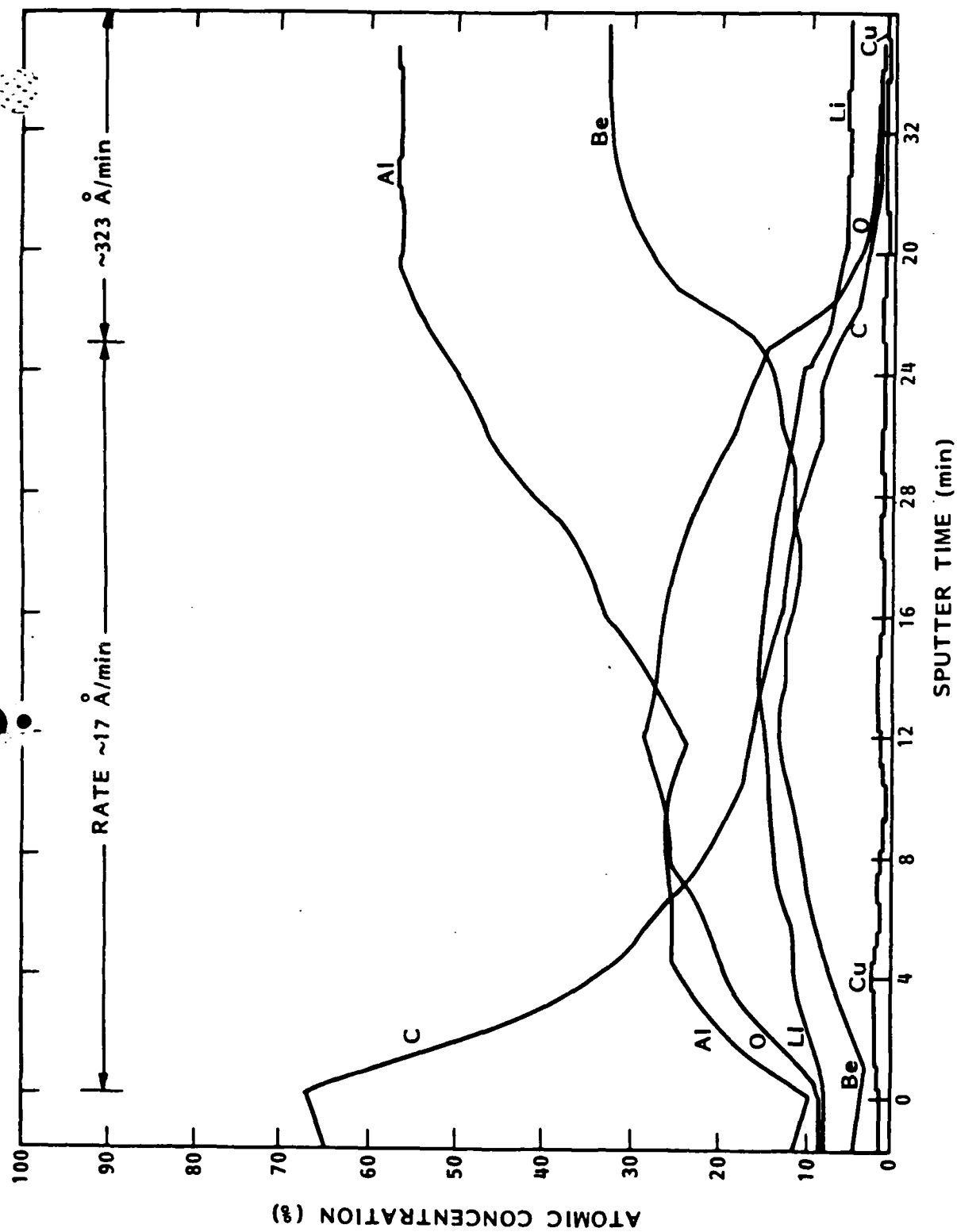


Figure 29 AES depth profile of a similar surface as in Figure 28 after oxidation at 500°C for 20 minutes in air.

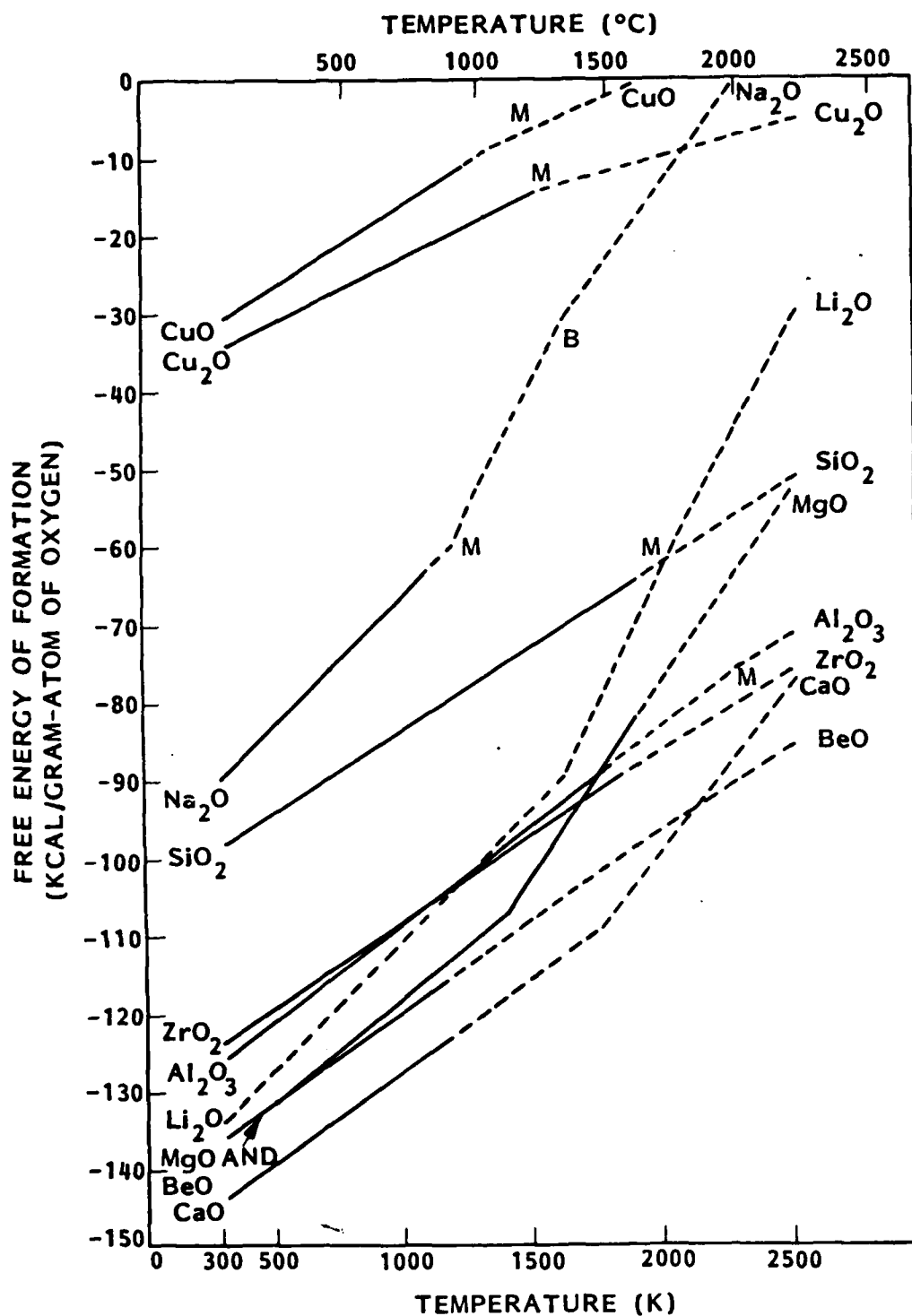


Fig. 30 Free Energies of formation of common oxides of interest (relative to Al-Li alloys).

**END**

**FILMED**

**10-85**

**DTIC**